Discrete and periodic complex Ginzburg-Landau equation for a hydrodynamic active lattice

Stuart J. Thomson, Matthew Durey, and Rodolfo R. Rosales

Phys. Rev. E **103**, 062215 — Published 25 June 2021

DOI: 10.1103/PhysRevE.103.062215

A discrete and periodic complex Ginzburg-Landau equation for a hydrodynamic active lattice

Stuart J. Thomson[1,2], Matthew Durey[2], and Rodolfo R. Rosales[2]

[1]School of Engineering, Brown University, Providence, RI 02912, USA

[2]Department of Mathematics, Massachusetts Institute of Technology, Cambridge, MA 02139, USA

Abstract

A discrete and periodic complex Ginzburg-Landau equation, coupled to a mean equation, is systematically derived from a driven and dissipative lattice oscillator model, close to the onset of a supercritical Andronov-Hopf bifurcation. The oscillator model is inspired by recent experiments exploring active vibrations of quasi-one-dimensional lattices of self-propelled millimetric droplets bouncing on a vertically vibrating fluid bath. Our systematic derivation provides a direct link between the constitutive properties of the lattice system and the coefficients of the resultant amplitude equations, paving the way to compare the emergent nonlinear dynamics—namely the onset and formation of discrete dark solitons, breathers, and traveling waves—against experiments. The framework presented herein is expected to be applicable to a wider class of oscillators characterized by the presence of a dynamic coupling potential between particles. More broadly, our results point to deeper connections between nonlinear oscillators and the physics of active and driven matter.

1 Introduction

With origins in the macroscopic theory of superconductivity [1, 2, 3, 4], the celebrated complex Ginzburg-Landau equation (CGLE) [5, 6] is a generic model describing the dynamics of spatially extended, dissipative systems near an Andronov-Hopf bifurcation. In contrast to the complex, high-dimensional microscopic equations regulating a particular physical system, amplitude equations [7, 8] such as the CGLE are typically cast in terms of only a few macroscopic variables, or order parameters [9, 10, 11, 12, 13]. In general, the form of such effective models may be posited on phenomenological grounds, their structure determined through a combination of linear stability and symmetry arguments [7]. This universal approach can, however, obfuscate the connection between the coefficients of the amplitude equation and the physical parameters of the system under study. Exemplified by the theory of hydrodynamic stability [14, 15, 16, 17], a more robust approach sacrifices derivational simplicity in favor of obtaining the amplitude equation(s) *directly* from the underlying microscopic equations of the system, typically continuous nonlinear partial differential equations [18]. In contrast, for systems that are fundamentally discrete, amplitude equations are typically posed as discretized versions of their continuous counterparts [19, 20, 21, 22, 23], seldom derived in a systematic manner from the original governing equations.

We herein present a rigorous framework to systematically derive a fundamentally discrete and periodic complex Ginzburg-Landau equation (dpCGLE), coupled to a discrete and periodic mean equation, for a driven and dissipative nonlinear oscillator, close to the onset of a supercritical Andronov-Hopf bifurcation. The oscillator model is inspired by recent experiments exploring the active vibrations of a hydrodynamic lattice of self-propelled millimetric droplets bouncing on a vertically vibrating fluid bath [24, 25]. The coefficients appearing in our dpCGLE are directly related to the constitutive properties of the physical lattice system, paving the way to compare the emergent nonlinear dynamics of the amplitude equations—namely the onset and formation of discrete dark solitons, breathers, and traveling waves—against experiments. Although we present the case of the hydrodynamic lattice, we propose that the framework presented herein is applicable to a wider class of oscillators characterized by the presence of a *dynamic* coupling potential between particles.

On a fundamental level, our results suggest deeper connections between nonlinear oscillators and the physics of active and driven matter [12, 26, 27].

1.1 The hydrodynamic active lattice

This study is motivated by experiments of quasi-one-dimensional lattices of millimetric droplets, bouncing synchronously and periodically on the surface of a vertically vibrating fluid bath and confined to an annular channel [24]; see Figure 1. (For a broader perspective of the physics of bouncing droplets, see [28, 29, 30, 31] and references therein.) Upon successive impacts, each droplet excites a field of standing waves whose decay time, T_M, increases with the vertical acceleration of the bath and diverges at the Faraday threshold [32, 33]. The superposition of the wave fields generated by each droplet forms the global lattice wave field, which acts as an inter-droplet potential, mediating the spatiotemporal coupling of the lattice. This wave-mediated coupling represents a distinguishing feature of this new class of coupled oscillator: the waves produced at each droplet impact give rise to an effective self-generated, *dynamic* coupling potential between droplets, one that evolves continuously with the droplet motion [34].

For sufficiently weak vibrational forcing, the droplets exhibit stationary bouncing in a circular, equispaced lattice. Above a critical vertical acceleration of the bath (or, alternatively, critical decay time, T_M), the droplets destabilize to small lateral perturbations, oscillating about their equilibrium position (see Figures 1b and 1c). Physically, these oscillations emerge due to the competition between droplet self-propulsion—arising through the propulsive force enacted on each droplet by the local slope of the lattice wave field—and wave-mediated, nonlocal coupling between droplets. Oscillations of the lattice are further offset by dissipative effects due to drag. That self-propulsion is achieved and sustained by the continual exchange of energy of the droplet with its environment—in this case, the vibrating bath—renders this hydrodynamic lattice a novel example of an inanimate active system. We note, however, that inertial effects [35, 36, 37, 38, 39] play a significant role in the droplet system, through both the finite mass of the droplets and the underdamped Faraday waves excited on each impact with the bath. These effects contrast with prevailing model systems of active and driven matter, such as bacterial or colloidal suspensions, where the particle

dynamics and their environment are typically overdamped [40].

As shown in experiments [24], oscillations of the lattice follow the onset of either a supercritical or subcritical Andronov-Hopf bifurcation, depending primarily on the proximity of neighboring droplets. Our focus here is on the supercritical case, for which periodic, small-amplitude, out-of-phase oscillations, initially uniform over all droplets, arise beyond a critical decay time of the waves. (When the bifurcation is subcritical, the dynamics is profoundly different: in experiments, the system approaches a distant attractor characterized by a self-sustaining, nonlinear solitary-like wave [24].) The dependence of the form of these bifurcations on the parameters of the lattice system, and the ensuing dynamics of the uniform, periodic state, was recently characterized *via* a weakly nonlinear analysis of a mathematical model describing the droplet lattice [25]. Upon further increase of the vibrational forcing, this periodic state can itself destabilize, leading to spatial modulations of the droplet oscillation amplitude, a phenomenon not captured by the analysis presented in [25]. To explore and rationalize the onset and resultant dynamics of these spatial modulations, we here present a generalized weakly nonlinear theory of the lattice, in the vicinity of the supercritical Andronov-Hopf bifurcation. We proceed in §§1.2–1.4 to briefly summarize the results of [25] as they pertain to our derivation of the governing amplitude equations presented herein; the results of our new generalized weakly nonlinear theory are summarized in §1.5.

1.2 Lattice model

The principal assumption underpinning the hydrodynamic lattice model [25] is that the horizontal motion of each of the N droplets in the lattice may be averaged over one bouncing period, which we denote T_F. This averaging, or *stroboscopic approximation* [41], eliminates the droplets' synchronous vertical motion from consideration. To further simplify matters, we assume that the droplets lie on a circle of constant radius, R, which, in experiments, is determined by the inner and outer radii of the annular channel. Combining this motion with the stroboscopic approximation yields the following equation of motion for the circumferential position, $x_n(t)$, of each droplet in the lattice [25]:

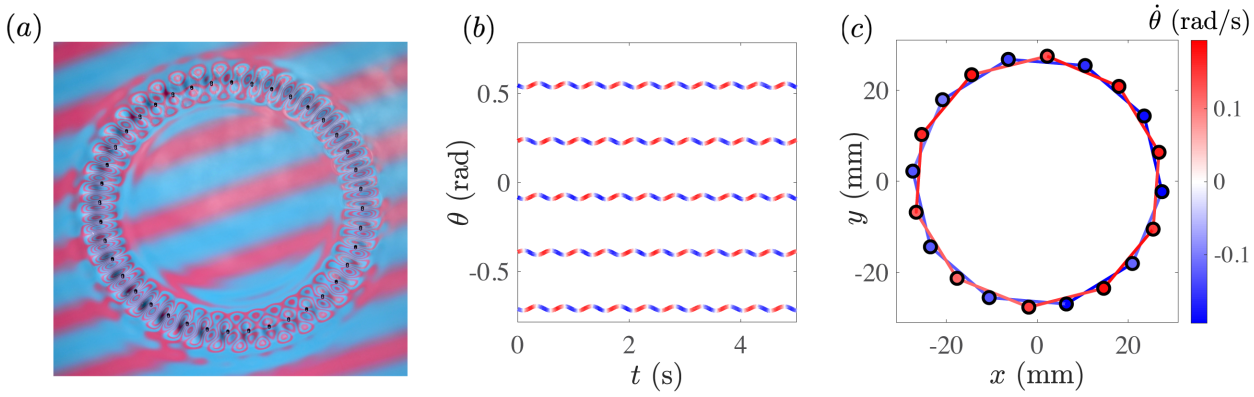

Figure 1: (a) Overhead perspective of a chain of 40 equispaced, millimetric droplets of silicone oil, confined to an annular channel and surrounded by a shallow layer of fluid. The reflected color in the channel emphasizes the deformation of the fluid surface as droplets impact the bath and excite subcritical Faraday waves. (b) A subset of droplet polar positions obtained from experiments for a lattice consisting of 20 droplets [24]. Each droplet undergoes out-of-phase oscillations with respect to its neighbor, following a supercritical Andronov-Hopf bifurcation [25]. (c) The instantaneous positions of all 20 droplets in the lattice for the same experiment as (b). The net result of the instability is the out-of-phase oscillations of two decahedral sub-lattices, colored red and blue.

$$m\ddot{x}_n + \bar{D}\dot{x}_n = -mg\frac{\partial h}{\partial x}(x_n, t). \tag{1a}$$

Dots denote differentiation with respect to time, t, and the space variable, $x \in [0, L = 2\pi R]$, is directed along the circumference of the circle on which the droplets lie. According to equation (1a), the time-averaged motion of each droplet of mass m is thus governed by a balance between inertia, a linear drag with drag coefficient $\bar{D}$, and the time-averaged propulsive wave force enacted on each droplet by the local slope of the lattice wave field, $h(x,t)$, at position $x = x_n$. By periodicity, $h(x,t) = h(x+L,t)$. The remaining parameter, g, is acceleration due to gravity. It is to be understood that $h(x,t)$ is the stroboscopic *global* lattice wave field—the time-averaged *superposition* of wave fields generated by each individual droplet in the lattice—projected onto the circle.

A distinguishing feature of the hydrodynamic lattice is that the propulsive wave force enacted on each droplet depends explicitly on the prior trajectory of *every* droplet in the lattice [25, 32, 33, 41]. The time-dependent evolution of the lattice wave field, h, may be described by

$$\frac{\partial h}{\partial t} + \frac{1}{T_M}h = \frac{1}{T_F}\sum_{m=1}^{N}\mathcal{H}(x - x_m), \tag{1b}$$

where the wave kernel, $\mathcal{H}(x)$, is the quasistatic wave field generated by stationary bouncing of each individual droplet, time-averaged over T_F and projected onto the circle [25]. Prompted by the fundamental aspects of the fluid system [24], our theory requires only that $\mathcal{H}(x)$ be even, sufficiently smooth, and periodic with $\mathcal{H}(x) = \mathcal{H}(x+L)$, exhibiting (i) variations over a characteristic wavelength $\lambda_W \ll L$ and (ii) exponential spatial decay localized about $x = 0$, with lengthscale $l_d \ll L$; see Figure 2(b) and §4 for a prototypical example. It is worth emphasizing here that the work in [25] shows that the droplet lattice spacing, L/N, for lattices which undergo a supercritical Andronov-Hopf bifurcation is on the same scale as λ_W (see §1.4 and Figure 2(c)). This, in turn, is the root cause that forces the need for a discrete Ginzburg-Landau equation. In summary, equation (1b) represents a balance between the rate-of-change of h, wave dissipation over the time scale T_M, and the superposition of waves generated about the instantaneous position of each droplet in the lattice.

The dynamical system (1) is non-dimensionalized *via* the scalings

$$t = \frac{m}{\overline{D}}\hat{t} = t_0\hat{t}, \qquad x = \lambda_W\hat{x}, \qquad h = \frac{\lambda_W^2}{gt_0^2}\hat{h} = h_0\hat{h}, \qquad \mathcal{H} = \frac{h_0 T_F}{t_0}\hat{\mathcal{H}}.$$

Upon dropping the carets, we arrive at the dimensionless lattice system [25]

$$\ddot{x}_n + \dot{x}_n = -\frac{\partial h}{\partial x}(x_n, t), \tag{2a}$$

$$\frac{\partial h}{\partial t} + \nu h = \sum_{m=1}^{N} \mathcal{H}(x - x_m), \tag{2b}$$

where $\nu = t_0/T_M$ is the dimensionless dissipation rate of the wave field. Recalling that the decay time, T_M, may be regarded as a proxy for the vertical vibrational acceleration of the bath [32, 33], ν plays the role of a control, or bifurcation, parameter in the dimensionless system (2). While ν is convenient for algebraic manipulations, we will interpret our results in terms of the dimensionless *memory parameter*, $M = 1/\nu$, where the influence of prior droplet dynamics increases with M. For future reference, we provide a list of the salient dimensionless parameters related to the lattice model (2) in Table 1.

1.3 Linear stability of the equispaced lattice

The critical value of M above which the wave force promotes sustained self-propulsion of the droplets, and hence oscillations of the lattice, is determined from the linear stability of the lattice system (2). We summarize the key results; full details are presented in [25].

Coinciding with experiments [24], we consider the stability of a static, equispaced lattice with droplet positions $x_n = n\delta$ and corresponding free-surface elevation $h = \nu^{-1}\sum_{m=1}^{N}\mathcal{H}(x - m\delta)$, where $\delta = 2\pi r_0/N$ is the droplet arc-length separation along the circle of dimensionless radius $r_0 = R/\lambda_W$. The droplet positions are subject to small perturbations of the form

$$x_n(t) = n\delta + \eta\left[A\exp(\mathrm{i}kn\alpha + \lambda_k t) + \text{c.c.}\right], \quad \eta \ll 1, \tag{3}$$

with a concomitant perturbation to the wave field, h. Here $\alpha = 2\pi/N$ is the angular spacing of the droplets, A is a complex amplitude, i is the imaginary unit, and c.c. denotes complex conjugation of the preceding term. The eigenvalues, λ_k, for each integer wavenumber, k, satisfy the dispersion relation $\mathcal{D}_k(\lambda_k;\nu) = 0$ [25], where

$$\mathcal{D}_k(\lambda_k;\nu) = \lambda_k^2 + \lambda_k + \frac{c_0}{\nu} - \frac{c_k}{\lambda_k + \nu} \tag{4}$$

Parameter	Definition
Lattice model (2)	
x_n	droplet positions
N	number of droplets
h	stroboscopic lattice wave field
$\mathcal{H}$	single-droplet, quasistatic wave kernel with characteristic wavelength λ_W, decay length l_d, and amplitude $\mathcal{A}$
$\alpha = 2\pi/N$; $\delta = \alpha R/\lambda_W = \alpha r_0$	droplet angular separation; droplet arc-length separation
$l = l_d/\lambda_W$	dimensionless spatial decay length of wave kernel
ν; $M = 1/\nu$	dissipation rate of wave field; memory parameter
$\varepsilon = \sqrt{\nu_c - \nu}$; $\nu_c = 1/M_c$	perturbation parameter; instability threshold for supercritical Andronov-Hopf bifurcation
k_c; ω_c	critical wavenumber; angular frequency at supercritical Andronov-Hopf bifurcation
Amplitude equations (8)	
$\mu = \alpha/\varepsilon$; μ_c	bifurcation parameter for amplitude equations; threshold for onset of spatial modulations
A_n; B_n	nth droplet oscillation amplitude; rotational drift
c_g; σ_i; γ_i; D_i	group velocity parameter; growth coefficients; coupling coefficients; diffusion coefficients

Table 1: List of salient parameters in the lattice model (2), amplitude equations (8), and stability analysis thereof.

and the real constants c_k are defined as

$$c_k = \sum_{n=1}^{N} \cos(kn\alpha)\mathcal{H}''(n\delta).$$

By symmetry considerations, we need only consider discrete wavenumbers in the interval $k \in [0, \overline{N}]$, where $\overline{N} = \lfloor N/2 \rfloor$ and $\lfloor \cdot \rfloor$ denotes the floor function.

The equispaced lattice may destabilize *via* two distinct mechanisms, depending primarily on the droplet separation, δ [25]: (i) a so-called *geometric instability*, independent of the memory parameter, M, brought on by geometrical frustration of the lattice wave field; or (ii) an *oscillatory instability*, where, for some wavenumber k_c, the real part of a pair of complex-conjugate eigenvalues transitions from negative to positive as M increases through a critical value $M_c = 1/\nu_c$. We focus our attention in this paper on case (ii), which arises when $c_k \leq c_0$ for all k [25]. We note, however, that a fundamental property of the lattice system is its rotational invariance, characterized by the neutrally stable eigenvalue $\lambda_0 = 0$. As we shall see in §1.5, this invariance gives rise to a discrete and periodic mean equation coupled to our dpCGLE, resulting in a system describing the rotational drift of the lattice superimposed on the collective droplet oscillations. In Figure 2(a), we present an oscillatory instability arising for $N = 20$ droplets: as the control parameter, M, is increased, a single wavenumber $k_c = N/2$ first satisfies $\mathrm{Re}(\lambda_{k_c}) = 0$ for some critical value of $M = M_c$, with $\mathrm{Im}(\lambda_{k_c}) = \pm\omega_c$ and $\omega_c = \sqrt{c_0 M_c + 1/M_c}$.

1.4 Weakly nonlinear dynamics of spatially uniform oscillations

In the case of an oscillatory instability, that the system destabilizes to a pair of complex-conjugate eigenvalues points to an Andronov-Hopf bifurcation [25, 42]. The existence of an Andronov-Hopf bifurcation was confirmed in [25] by an accompanying weakly nonlinear stability analysis of the equispaced lattice. The analysis presented in [25] demonstrates that, in the vicinity of the critical memory ($0 < M - M_c \ll 1$), each droplet evolves according to

$$x_n = n\delta + [D(T) + O(\varepsilon)] + \varepsilon \left[A(T)\mathrm{e}^{\mathrm{i}(k_c n\alpha + \omega_c t)} + \text{c.c.}\right] + O(\varepsilon^2), \tag{5}$$

where $0 < \varepsilon = \sqrt{\nu_c - \nu} \ll 1$. The slowly varying complex amplitude, $A(T)$, a function of the slow timescale $T = \varepsilon^2 t$, is governed by a Stuart-Landau equation

$$\frac{\mathrm{d}A}{\mathrm{d}T} = \sigma_1 A - \bar{\sigma}_2 |A|^2 A \tag{6a}$$

with an accompanying equation governing the evolution of the rotational drift, D, of the lattice, namely

$$\frac{\mathrm{d}D}{\mathrm{d}T} = \bar{\gamma}_3 |A|^2. \tag{6b}$$

The origin of this rotational drift may be traced back to the neutrally stable $k = 0$ mode of the dispersion relation (4), corresponding to rotational invariance. As alluded to in §1.3, we will find an analogous equation in the amplitude equations presented in §1.5.

The coefficients σ_1, $\bar{\sigma}_2 \in \mathbb{C}$, and $\bar{\gamma}_3 \in \mathbb{R}$ in equations (6) are defined in terms of the parameters of the lattice system (2) [25], and are related to the coefficients of the amplitude equations derived here in §1.5. For now, we simply comment that the direction of rotational drift is given by the sign of $\bar{\gamma}_3$, changing direction when $\omega_c \to -\omega_c$. (Prompted by experimental observations, note that we only consider unidirectional waves in equation (5).) However, when $k_c = N/2$, it is found that $\bar{\gamma}_3 \equiv 0$, in which case $D =$ constant, corresponding to an arbitrary shift of the droplet equilibrium positions. Further, consistent with the instability of the equispaced lattice for $\nu < \nu_c$, we have that $\mathrm{Re}(\sigma_1) > 0$; hence the lattice undergoes a super- or sub-critical Andronov-Hopf bifurcation for $\mathrm{Re}(\bar{\sigma}_2) > 0$ and $\mathrm{Re}(\bar{\sigma}_2) < 0$, respectively.

The stability of the equispaced lattice and its complex dependence on the separation distance, δ, and dimensionless spatial decay length, $l = l_d/\lambda_W$, is summarized in Figure 2(c) for the particular case of $N = 20$ droplets. A crucial feature of the stability analysis just described is the value of the critical wavenumber, k_c [25]. When the Andronov-Hopf bifurcation is supercritical (green regions), it is typically observed that $k_c = \lfloor N/2 \rfloor$ (except near the boundaries with subcritical Andronov-Hopf bifurcations) [25]. As discussed in §2.3, we exploit this proximity to $k_c = N/2$ in our asymptotic derivation of the amplitude equations to capture relevant terms promoted from lower orders that should appear in our dpCGLE and mean equation.

The analysis presented in [25] accounts for *spatially uniform* oscillations of the lattice in

a small window ($0 < M - M_c \ll 1$) beyond the supercritical Andronov-Hopf bifurcation. However, numerical simulations of the hydrodynamic active lattice (2) reveal the onset of a second bifurcation as the memory parameter, M, is further increased, where the spatially uniform, small-amplitude oscillations of the droplet positions give way to spatio-temporal modulations in the droplet oscillation amplitude, arising *via* a long-wavelength instability [25]. To capture this second bifurcation, and the ensuing dynamics, the weakly nonlinear analysis leading to the amplitude equations (6) must be generalized to account for spatial, as well as temporal, effects.

1.5 The amplitude equations governing the lattice vibrations

Starting from the lattice system (2), we use the asymptotic method of multiple scales [43] to derive a generalized set of amplitude equations, accounting for both spatial and temporal modulations of the droplet oscillation amplitude and rotational drift. Specifically, we show that each droplet position evolves according to

$$x_n = n\delta + \varepsilon \left[A_n(T) \mathrm{e}^{\mathrm{i}(k_c n\alpha + \omega_c t)} + \text{c.c.} + B_n(T) \right] + O(\varepsilon^2), \tag{7}$$

where A_n is the slowly varying complex amplitude of the nth droplet in the lattice, B_n is the rotational drift, and $T = \varepsilon^2 t$ is the slow time scale. We emphasize that, in contrast to equation (5), the complex amplitude, A_n, and rotational drift, B_n, now depend on the droplet number, n. Moreover, spatial periodicity of the lattice implies that A_n and B_n are defined as periodic sequences, specifically $A_n = A_{n+N}$ and $B_n = B_{n+N}$ for all n.

As is typical in the method of multiple scales, eliminating secular terms at successive orders of ε yields a coupled system of equations for A_n and B_n, resulting in a dpCGLE coupled to a discrete and periodic mean equation:

$$\frac{\mathrm{d}A_n}{\mathrm{d}T} + \mu^2 c_g \nabla A_n = \sigma_1 A_n - \sigma_2 |A_n|^2 A_n + \mu\gamma_1 A_n \nabla B_n + \mu^2 D_1 \Delta A_n, \tag{8a}$$

$$\frac{\mathrm{d}B_n}{\mathrm{d}T} = \mu^2 D_2 \Delta B_n + 2\mu \mathrm{Re}\left[\gamma_2 A_n \nabla A_n^*\right] + \mu\gamma_3 |A_n|^2. \tag{8b}$$

Our analysis leads us to define the control parameter, μ, appearing in the amplitude equations (8), defined by

$$\mu = \frac{\alpha}{\varepsilon} = \frac{2\pi}{N\sqrt{\nu_c - \nu}}.$$

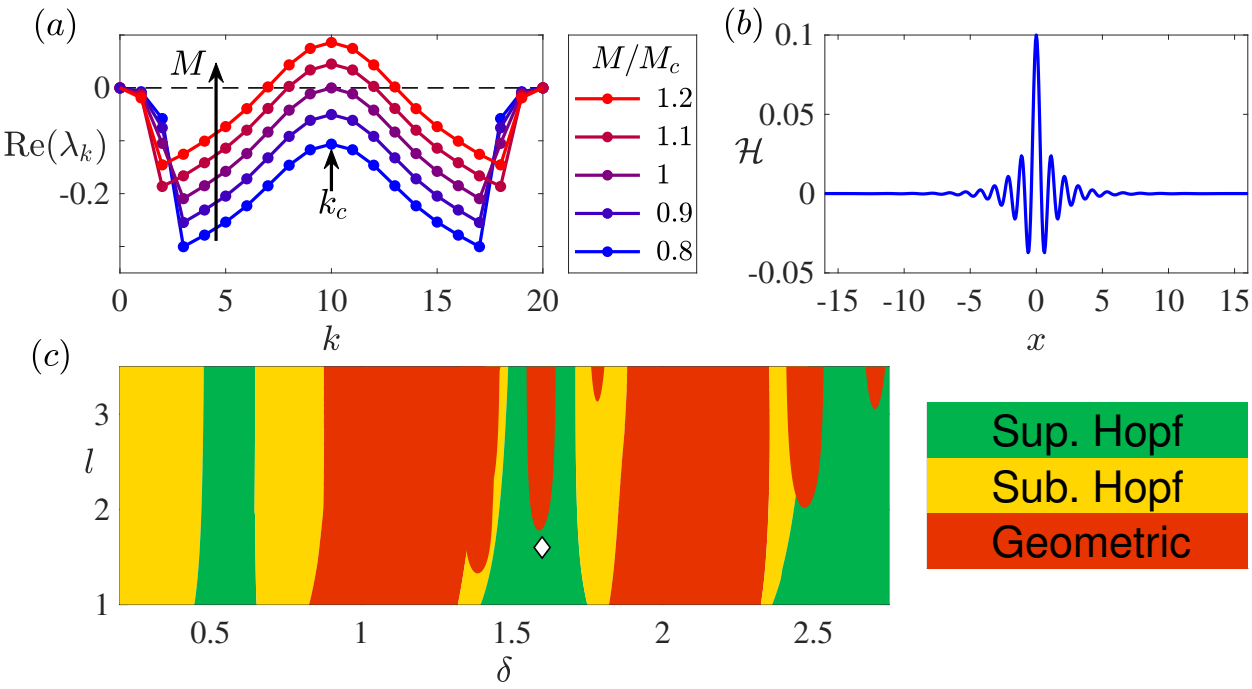

Figure 2: (a) Behavior of the real part of the eigenvalues, λ_k, of the equispaced lattice (computed from (4)) in the case of a supercritical Andronov-Hopf bifurcation for $N = 20$ droplets. At a critical memory, $M = M_c$, a single non-zero, integer wavenumber $k_c = 10$ first satisfies $\mathrm{Re}(\lambda_{k_c}) = 0$. The solid curves joining the discrete values of $\mathrm{Re}(\lambda_k)$ for each integer k are used as visual guides. (b) The prototypical wave-field kernel, $\mathcal{H}(x)$, used in numerical simulations presented herein (see §4 for details). (c) Regime diagram summarizing the stability of an equispaced lattice of $N = 20$ droplets as the parameters l and δ are varied independently [24, 25], as derived from (4) and (6). We delineate regimes of super- and sub-critical Andronov-Hopf bifurcations, as well as geometric frustration of the equispaced lattice [25]. The diamond indicates the parameter values used in (a) and (b), specifically $\delta = l = 1.6$.

Our theory is valid for $\mu = O(1)$ or, equivalently, for the dominant balance $\alpha \sim \varepsilon \ll 1$. (We note that this condition requires that N be sufficiently large.) Table 1 provides a reference list of coefficients appearing in the amplitude equations (8).

Central to the amplitude equations (8) are the first and second-order difference operators, ∇ and Δ, which may be regarded as the discrete counterparts of spatial derivatives.

As detailed in §2.2, these difference operators are defined in terms of the discrete Fourier transform (DFT). Specifically, for a periodic sequence $F_n = F_{n+N}$ for all n, we first define the DFT [44]

$$\mathscr{F}_\xi[F_n] = \sum_{n=0}^{N-1} F_n \mathrm{e}^{-\mathrm{i}n\xi\alpha} \quad \text{for} \quad \xi = 0, \ldots, N-1, \tag{9a}$$

and its inverse

$$\mathscr{F}_n^{-1}[\hat{F}_\xi] = \frac{1}{N} \sum_{\xi=0}^{N-1} \hat{F}_\xi \mathrm{e}^{\mathrm{i}n\xi\alpha} \quad \text{for} \quad n = 0, \ldots, N-1, \tag{9b}$$

where we denote $\hat{F}_\xi = \mathscr{F}_\xi[F_n]$. We then define the difference operators, ∇ and Δ, in terms of their Fourier symbols, $\hat{\nabla}_\xi$ and $\hat{\Delta}_\xi$, so that $\mathscr{F}_\xi[\nabla F_n] = \hat{\nabla}_\xi \hat{F}_\xi$ and $\mathscr{F}_\xi[\Delta F_n] = \hat{\Delta}_\xi \hat{F}_\xi$, or, equivalently,

$$\nabla F_n = \sum_{m=1}^{N} F_m \mathscr{F}_{n-m}^{-1}[\hat{\nabla}_\xi] \quad \text{and} \quad \Delta F_n = \sum_{m=1}^{N} F_m \mathscr{F}_{n-m}^{-1}[\hat{\Delta}_\xi].$$

Finally, the periodic Fourier symbols, $\hat{\nabla}_\xi$ and $\hat{\Delta}_\xi$ (satisfying $\hat{\nabla}_\xi = \hat{\nabla}_{\xi+N}$ and $\hat{\Delta}_\xi = \hat{\Delta}_{\xi+N}$), are derived in §2.2 and are defined $\hat{\nabla}_\xi = \mathrm{i}\xi$ for $|\xi| < N/2$ and $\hat{\Delta}_\xi = -\xi^2$ for $|\xi| \leq N/2$. We define $\hat{\nabla}_{N/2} = 0$ so that the associated difference operator, ∇, is real when N is even [44].

We pause to emphasize a few aspects of the system (8). With regards to the coefficients, the group velocity parameter, c_g, growth coefficients, σ_i $(i = 1, 2)$, coupling coefficients, γ_i $(i = 1, 2, 3)$, and the diffusion coefficients, D_i $(i = 1, 2)$, are determined as part of the multiple scales analysis and are directly related to the physical parameters of the lattice system (2) (see Appendix A for their algebraic forms). Notably, $D_2 > 0$ and γ_3 are both real, while the remaining parameters are all complex with $\mathrm{Re}(\sigma_1) > 0$ and $\mathrm{Re}(D_1) > 0$.

Next, we highlight a key assumption involved in deriving the amplitude equations (8) that was not present in deriving the spatially uniform Stuart-Landau and drift equations (6): namely that $\alpha \ll 1$, which is required for the concept of slow variation of A_n and B_n with n. A keen eye will note that equations (8) do not immediately reduce to equations (6) when solutions independent of n are considered. However, consistency between (8) and (6) is achieved in the limit $\alpha \to 0$ when spatial variations are absent, since we find that $\sigma_2 = \bar{\sigma}_2 + O(\alpha)$. Further, as discussed in Appendix A, $\bar{\gamma}_3 = \alpha\gamma_3 = O(\alpha)$ when $k_c \lesssim \lfloor N/2 \rfloor$, and hence the drift, D, appearing in the expansion (5) is promoted to $O(\varepsilon)$ when $\alpha \sim \varepsilon \ll 1$; consequently, D is replaced by εB_n in the expansion (7).

Finally, we note that, in our system, discreteness originates at the level of the underlying microscopic equations (2), and thus is a connate characteristic of the resultant amplitude equations (8). This fundamental discreteness is in contrast with discrete versions of the CGLE motivated by a direct discretization of the continuous CGLE using standard finite difference operators [20, 21, 22, 23]. Similarly, periodicity arises from the periodicity of the lattice, rather than being later imposed through periodic boundary conditions [45, 46]. Interestingly, the system (8) is the discrete and periodic analogue of the amplitude equations describing a host of disparate physical phenomena presented elsewhere [47, 48, 49, 50].

1.6 Outline

This paper is organized as follows. For the interested reader, in §2 we provide further details of the multiple scales procedure involved in deriving the amplitude equations (8) from the lattice model (2). We then proceed to analyze the successive bifurcations of the amplitude equations (8) in §3, rationalizing the onset of the second bifurcation leading to a long-wavelength instability of time-periodic oscillations of the lattice. Numerical solutions of the amplitude equations (8) beyond the second bifurcation are presented in §4, demonstrating their rich dynamical behavior in the form of traveling waves, dark solitons and dark breathers, prompting future comparison with experiments. A review of our results is presented in §5, along with a discussion of future directions.

2 Mechanics of the weakly nonlinear analysis

The weakly nonlinear analysis leading to the derivation of the amplitude equations (8) assumes slowly varying spatial and temporal modulations of the oscillation amplitude and rotational drift of each droplet. For a supercritical Andronov-Hopf bifurcation, stable, small-amplitude oscillations arise when ν is only slightly below the critical threshold, ν_c (corresponding to M slightly above M_c); specifically we consider $0 < \varepsilon = \sqrt{\nu_c - \nu} \ll 1$ and small perturbations from the equispaced lattice configuration $x_n = n\delta$ and $h = \nu_c^{-1} \sum_{m=1}^{N} \mathcal{H}(x -$

$m\delta$). We then pose the following asymptotic multiple-scales expansions

$$x_n \sim n\delta + \sum_{i=1}^{\infty} \varepsilon^i x_n^{(i)}(t,T), \quad h \sim \frac{1}{\nu_c} \sum_{m=1}^{N} \mathcal{H}(x - m\delta) + \sum_{i=1}^{\infty} \varepsilon^i h^{(i)}(x,t,T), \tag{10}$$

where the slow time-scale is $T = \varepsilon^2 t$.

As described fully in Appendix A, inserting (10) into the lattice system (2) leads to a hierarchy of problems for $x_n^{(i)}$ and $h^{(i)}$ at successive orders of ε. A series of solvability conditions must then be satisfied at each order of ε to guarantee the suppression of secular terms that would otherwise lead to unbounded solutions and a violation of the multiple-scales *ansatz* (10). Satisfying the solvability condition arising at $O(\varepsilon^3)$ leads to the amplitude equations (8). Before arriving there, however, there are several aspects of the current problem that complicate the weakly nonlinear, multiple-scales analysis of the lattice system (2). Our derivation falls into three stages: (i) we first solve for the wave-field perturbations, $h^{(i)}$, allowing us to project the wave force onto the droplet trajectories, $x_n^{(i)}$; (ii) we next exploit the spatial decay of the wave kernel, $\mathcal{H}$, and the assumed slowly varying spatial effects to develop an asymptotic approximation of the nonlocal inter-droplet coupling; (iii) finally, we consider the limit of weak asymmetry when the number of droplets is large (equivalently, when k_c departs slightly from $N/2$). We elaborate on these three *key ideas* below.

2.1 Solving for the wave field

Our first point of interest is at $O(\varepsilon)$, where the lattice equations (2) yield

$$\frac{\partial^2 x_n^{(1)}}{\partial t^2} + \frac{\partial x_n^{(1)}}{\partial t} = -\frac{x_n^{(1)}}{\nu_c} \sum_{m=1}^{N} \mathcal{H}''((n-m)\delta) - \left.\frac{\partial h^{(1)}}{\partial x}\right|_{x=n\delta}, \tag{11a}$$

$$\frac{\partial h^{(1)}}{\partial t} + \nu_c h^{(1)} = -\sum_{m=1}^{N} x_m^{(1)} \mathcal{H}'(x - m\delta). \tag{11b}$$

At this stage in conventional multiple-scales analyses of nonlinear oscillators [42, 43], one is typically interested in solving for the perturbed oscillator position, $x_n^{(1)}$, alone. In the present case, however, we must also contend with equation (11b) governing the free-surface perturbation, $h^{(1)}$. In order to project the dynamics entirely onto the droplet trajectories, $x_n^{(1)}$, our *first key idea* is to use the form of (11b) to define the auxiliary variables, X_n,

satisfying [25]

$$\frac{\partial X_n}{\partial t} + \nu_c X_n = x_n^{(1)}. \tag{12}$$

A particular solution of (11b) is then

$$h^{(1)} = -\sum_{m=1}^{N} X_m \mathcal{H}'(x - m\delta). \tag{13}$$

We neglect the homogeneous solution of (11b), which decays exponentially on the fast time-scale, t [25]. Now that $h^{(1)}$ is expressed in terms of the auxiliary variables, X_n, through equation (13), the linear system (11) may be recast as a dynamical system for $x_n^{(1)}$ and X_n. Specifically, substituting (13) into (11a) yields $\mathcal{L}_n \boldsymbol{x}^{(1)} = 0$, where $\boldsymbol{x}^{(1)} = \left(x_1^{(1)}, \ldots, x_N^{(1)}\right)$ and the linear operator, $\mathcal{L}_n$, is defined as

$$\mathcal{L}_n \boldsymbol{x}^{(1)} = \frac{\partial^2 x_n^{(1)}}{\partial t^2} + \frac{\partial x_n^{(1)}}{\partial t} + \sum_{m=1}^{N} \left(\frac{x_n^{(1)}}{\nu_c} - X_m \right) \mathcal{H}''(\delta(n-m)). \tag{14}$$

Informed by the *ansatz* (3), we now seek a solution to $\mathcal{L}_n \boldsymbol{x}^{(1)} = 0$ of the form

$$x_n^{(1)} = A_n(T) \mathrm{e}^{\mathrm{i}(k_c n\alpha + \omega_c t)} + \text{c.c.} + B_n(T), \quad X_n = \frac{A_n(T)}{\nu_c + \mathrm{i}\omega_c} \mathrm{e}^{\mathrm{i}(k_c n\alpha + \omega_c t)} + \text{c.c.} + \frac{1}{\nu_c} B_n(T), \tag{15}$$

where we recall that the critical wavenumber of instability, k_c, and angular frequency, ω_c, are determined from linear theory (§1.3). We note that the presence of the subscript n in both the complex amplitude, A_n, and mean, B_n, generalizes the spatially uniform expansion (5) considered in prior work [25], which leads to the derivation of the Stuart-Landau equation (6a) and the drift equation (6b). By inserting (15) into (14), we find that

$$\mathcal{L}_n \boldsymbol{x}^{(1)} = \left\{ \frac{\mathrm{e}^{\mathrm{i}\phi_n}}{\nu_c + \mathrm{i}\omega_c} \sum_{m=1}^{N} (A_n - A_{n-m}) \mathrm{e}^{-\mathrm{i}k_c m\alpha} \mathcal{H}''(m\delta) \right\} + \text{c.c.} \\ + \frac{1}{\nu_c} \sum_{m=1}^{N} (B_n - B_{n-m}) H''(m\delta), \tag{16}$$

where $\phi_n = k_c n\alpha + \omega_c t$. We note that, *en route* to obtaining (16), we first write $A_{n-m} = (A_{n-m} - A_n) + A_n$ and then simplify the resultant expression using the properties of the dispersion relation, namely $\mathcal{D}_{k_c}(\lambda_{k_c}; \nu_c) = \mathcal{D}_0(0; \nu_c) = 0$.

2.2 Approximating discrete convolutions

We now arrive at the *second key idea*, which lies at the heart of our analysis: approximating the discrete convolutions arising in equation (16). When A_n and B_n are spatially uniform (i.e. independent of n), the right-hand side of (16) is identically zero. To allow for spatial variations, we approximately satisfy (16) at this order by considering the leading-order terms of an asymptotic expansion of each discrete convolution in terms of $\alpha \ll 1$, where $\alpha = 2\pi/N$ is the angular spacing parameter. We then assume a distinguished limit between the relative sizes of α and ε; specifically, we consider $\alpha \sim \varepsilon$ and thus define $\alpha = \mu\varepsilon$, where $\mu = O(1)$ is the control parameter appearing in the amplitude equations (8).

Motivated by the discrete convolutions appearing in (16), we proceed to derive an asymptotic expansion for the convolution

$$I_n = \sum_{m=1}^{N} F_{n-m} G_m$$

in terms of the small parameter $\alpha \ll 1$, where $F_n = F_{n+N}$ and $G_n = G_{n+N}$ are given periodic sequences. For the active lattice under consideration, F_n plays the role of the complex amplitude, A_n, or the drift, B_n, while G_n plays the role of $\mathcal{H}''(n\delta)$, or similarly for higher-order derivatives of $\mathcal{H}$. We therefore suppose that F_n is slowly varying in n, resulting in its DFT, $\hat{F}_\xi$, being localized around $\xi = 0$. We consider here the regime where the exponential decay length of the wave kernel, $\mathcal{H}$, is comparable to the droplet separation distance, so $\delta \sim l$. As a consequence, G_n may be assumed to be localized around $n = 0$, resulting in $\hat{G}_\xi$ being slowly varying in ξ.

By the convolution theorem, it follows that $\hat{I}_\xi \equiv \mathscr{F}_\xi[I_n]$ satisfies $\hat{I}_\xi = \hat{F}_\xi \hat{G}_\xi$. As $\hat{F}_\xi$ is localized around $\xi = 0$, we aim to expand $\hat{G}_\xi$ about $\xi = 0$ with $\xi = O(1)$. We first recast the DFT (9a) as

$$\hat{G}_\xi = \sum_{n \in \mathcal{I}} G_n \mathrm{e}^{-\mathrm{i}n\xi\alpha} \quad \text{for} \quad \xi \in \mathcal{I},$$

where the set $\mathcal{I}$ is defined $\mathcal{I} = \{-\frac{1}{2}N, \ldots, \frac{1}{2}N-1\}$ for N even and $\mathcal{I} = \{-\frac{1}{2}(N-1), \ldots, \frac{1}{2}(N-1)\}$ for N odd. We then Taylor expand

$$\mathrm{e}^{-\mathrm{i}n\xi\alpha} \sim 1 - \mathrm{i}n\alpha\xi - \frac{1}{2}n^2\alpha^2\xi^2 + O(\alpha^3),$$

valid for $n, \xi = O(1)$. By exploiting the assumed exponential localization of G_n around $n = 0$, we obtain

$$\hat{G}_\xi \sim \sum_{n\in\mathcal{I}} G_n \left[1 - \mathrm{i}n\alpha\xi - \frac{1}{2}n^2\alpha^2\xi^2\right] + O(\alpha^3),$$

valid for $\xi = O(1)$, incurring only exponentially small errors when including terms with $n \neq O(1)$ in the sum. It then follows that

$$\hat{I}_\xi \sim \hat{F}_\xi \sum_{n\in\mathcal{I}} G_n - \alpha(\mathrm{i}\xi\hat{F}_\xi) \sum_{n\in\mathcal{I}} nG_n + \alpha^2(-\xi^2\hat{F}_\xi) \sum_{n\in\mathcal{I}} \frac{n^2}{2} G_n + O(\alpha^3) \tag{17}$$

for $\xi \in \mathcal{I}$, where we again incur only exponentially small errors when $\xi \neq O(1)$ due to the exponential localization of $\hat{F}_\xi$ around $\xi = 0$.

By applying the inverse DFT (9b) to equation (17), we obtain the asymptotic expansion

$$I_n \sim F_n \sum_{m=1}^{N} G_m - \alpha\nabla F_n \sum_{m=1}^{N} a_m G_m + \alpha^2 \Delta F_n \sum_{m=1}^{N} b_m G_m + O(\alpha^3), \tag{18}$$

where the difference operators, ∇ and Δ, are defined in §1.5. Finally, the weights a_n and b_n are periodic in n (so $a_n = a_{n+N}$ and $b_n = b_{n+N}$) and are defined as $a_n = n$ for $|n| < \frac{1}{2}N$ and $b_n = \frac{1}{2}n^2$ for $|n| \leq \frac{1}{2}N$. We define $a_{N/2} = 0$ to avoid bias arising in the sum $\sum_{n\in\mathcal{I}} nG_n$ when N is even, since one could equally include $n = -N/2$ or $n = +N/2$ in the set $\mathcal{I}$. Setting $a_{N/2} = 0$ incurs only exponentially small errors in the sum $\sum_{m=1}^{N} a_m G_m$ due to the exponential localization of G_m around $m = 0$. We note that, under these definitions, a_n is an odd sequence in n, while b_n is an even sequence in n.

Applying the asymptotic expansion (18) to the convolutions in (16) yields the sought-after approximation

$$\mathcal{L}_n \boldsymbol{x}^{(1)} + \left\{ -\alpha \frac{\nabla A_n \mathrm{e}^{\mathrm{i}\phi_n}}{\nu_c + \mathrm{i}\omega_c} \sum_{m=1}^{N} a_m \mathrm{e}^{-\mathrm{i}k_c m\alpha} \mathcal{H}''(m\delta) + \alpha^2 \frac{\Delta A_n \mathrm{e}^{\mathrm{i}\phi_n}}{\nu_c + \mathrm{i}\omega_c} \sum_{m=1}^{N} b_m \mathrm{e}^{-\mathrm{i}k_c m\alpha} \mathcal{H}''(m\delta) \right\} + \text{c.c.}$$
$$+ \alpha^2 \frac{\Delta B_n}{\nu_c} \sum_{m=1}^{N} b_m \mathcal{H}''(m\delta) = O(\alpha^3). \tag{19}$$

We note that there is not a ∇B_n term in (19) as the symmetry of the wave kernel, $\mathcal{H}$, and the oddness of the sequence, a_n, determines that its coefficient vanishes, specifically $\sum_{m=1}^{N} a_m \mathcal{H}''(m\delta) = 0$. Recalling our assumption that $\alpha \sim \varepsilon$, terms of $O(\alpha^n)$ in equation (19) are consequently promoted to $O(\varepsilon^{n+1})$, appearing as secular terms (either those constant

in t or proportional to $\mathrm{e}^{\mathrm{i}\phi_n}$) on the right-hand side of the expansion of equation (2a). Thus, the ΔA_n and ΔB_n terms in equation (19) are destined to become the diffusion-like terms in the amplitude equations (8).

2.3 The limit of weak asymmetry

Finally, our *third key idea* exploits the observed correspondence between $k_c \lesssim \lfloor N/2 \rfloor$ and the emergence of a supercritical Andronov-Hopf bifurcation (see Figure 2(a)). We first define $\chi = N/2 - k_c$, where we typically find that $\chi = 0$ or $\chi = 1/2$, and then observe that $\alpha\chi \ll 1$ for $\chi = O(1)$ and $\alpha \ll 1$. Then, by recalling that $\alpha = 2\pi/N$, we use the form $k_c = N/2 - \chi$ to recast the ∇A_n coefficient in (19) as

$$\frac{\alpha}{\nu_c + \mathrm{i}\omega_c} \sum_{m=1}^{N} a_m \mathrm{e}^{-\mathrm{i}k_c m\alpha} \mathcal{H}''(m\delta) = \frac{\mathrm{i}\alpha}{\nu_c + \mathrm{i}\omega_c} \sum_{m=1}^{N} a_m (-1)^m \sin(m\alpha\chi) \mathcal{H}''(m\delta),$$

which is an even function of α for $\chi > 0$, and vanishes for $\chi = 0$. In the former case, this coefficient is expected to be of size $O(\alpha^2)$ as $\alpha \to 0$, which may be verified numerically. Further, we are prompted to define the $O(1)$ complex group velocity parameter

$$\hat{c}_g = \frac{1}{\alpha} \sum_{m=1}^{N} \frac{a_m \mathrm{e}^{-\mathrm{i}k_c m\alpha} \mathcal{H}''(m\delta)}{\nu_c + \mathrm{i}\omega_c},$$

which vanishes when $k_c = N/2$. The parameter $\hat{c}_g$ is divided by a further coefficient to yield the c_g in (8); see Appendix A for clarification. (Note that $\mathrm{Re}(c_g)$ plays the role of a true group velocity, while $\mathrm{Im}(c_g)$ is related to the asymmetric growth rate of perturbations to k_c.) Since we consider $\alpha \sim \varepsilon$, we then acknowledge that the term $\alpha^2 \hat{c}_g \nabla A_n$ in (19) appears as a secular term at $O(\varepsilon^3)$, ultimately resulting in the advective term in our dpCGLE (8a). In this final step, equation (19) reduces to $\mathcal{L}_n \boldsymbol{x}^{(1)} = O(\varepsilon^3)$, verifying our *ansatz* for $x_n^{(1)}$.

2.4 Summary

As shown in Appendix A, a combination of the foregoing three key ideas is used to systematically derive the amplitude equations (8) from the lattice system (2). The time derivatives and the nonlinear coupling terms in (8) are obtained by eliminating higher-order secular terms, both those that are promoted from $O(\varepsilon^2)$ and others that appear at $O(\varepsilon^3)$. We now

proceed to analyze the stability of the amplitude equations (8), elucidating the second bifurcation leading to spatiotemporal modulations of the droplet oscillation amplitude and drift as the control parameter, μ, is decreased from infinity (corresponding to $\nu < \nu_c$).

3 Stability of periodic oscillations

As discussed in §1.4, we are concerned with the stability of the hydrodynamic lattice beyond the threshold of the supercritical Andronov-Hopf bifurcation, specifically for $\nu < \nu_c$, or equivalently, for $\mu < \infty$. In this section, we elucidate the mechanism leading to a modulational instability of the spatially uniform solution of the amplitude equations (8). The onset of spatial amplitude modulations in the canonical complex Ginzburg-Landau equation is the eponymous Benjamin-Feir-Newell (BFN) instability, after its discovery in describing the instability of periodic surface gravity (Stokes) waves [51, 52]. As we shall see, in our system, this instability takes a slightly different form due to the coupling of the complex amplitude, A_n, with the mean, B_n. In what follows, we conduct a linear stability of the amplitude equations (8), the computations for which are standard [6], but lengthy. We therefore highlight only the key features here.

3.1 Linear stability

A supercritical Andronov-Hopf bifurcation arising in the limit $\alpha \ll 1$ corresponds to $\mathrm{Re}(\sigma_2) > 0$. In this case, there exists a spatially uniform solution to (8) of the form

$$A_n^{(0)}(T) = \rho \exp(\mathrm{i}\Omega T) \quad \text{and} \quad B_n^{(0)}(T) = \mu\gamma_3\rho^2 T + \text{constant}, \tag{20}$$

where the modulus and angular frequency of the complex amplitude are

$$\rho = \sqrt{\mathrm{Re}(\sigma_1)/\mathrm{Re}(\sigma_2)} \quad \text{and} \quad \Omega = \mathrm{Im}(\sigma_1\sigma_2^*)/\mathrm{Re}(\sigma_2).$$

We now consider small perturbations about the spatially uniform state (20) of the form

$$A_n(T) = A_n^{(0)}(T)(1 + \overline{A}_n(T)), \quad B_n(T) = B_n^{(0)}(T) + \overline{B}_n(T),$$

where $0 < |\overline{A}_n| \sim |\overline{B}_n| \ll 1$. Substituting this *ansatz* into (8) and neglecting terms of quadratic order and higher, we obtain a linear system governing the perturbations $\overline{A}_n$ and

$\overline{B}_n$, supplemented by an additional equation for $\overline{A}_n^*$. The resulting linear system may then be diagonalized by applying a DFT in n (see equation (9a)). Specifically, we define $\hat{A}_\xi = \mathscr{F}_\xi[\overline{A}_n]$, $\hat{B}_\xi = \mathscr{F}_\xi[\overline{B}_n]$ and $\hat{C}_\xi = \mathscr{F}_\xi[\overline{A}_n^*]$, where $\xi = 0, \ldots, N-1$. Under this transformation, we obtain

$$\frac{\mathrm{d}\hat{\mathbf{A}}_\xi}{\mathrm{d}T} = \mathrm{M}_\xi(\mu)\hat{\mathbf{A}}_\xi, \tag{21}$$

where $\hat{\mathbf{A}}_\xi = (\hat{A}_\xi, \hat{B}_\xi, \hat{C}_\xi)^T$ and

$$\mathrm{M}_\xi(\mu) = \begin{pmatrix} -\mu^2 c_g \hat{\nabla}_\xi - \rho^2\sigma_2 + \mu^2 D_1 \hat{\Delta}_\xi & \mu\gamma_1\hat{\nabla}_\xi & -\rho^2\sigma_2 \\ \mu\rho^2(\gamma_2^*\hat{\nabla}_\xi + \gamma_3) & \mu^2 D_2\hat{\Delta}_\xi & \mu\rho^2(\gamma_2\hat{\nabla}_\xi + \gamma_3) \\ -\rho^2\sigma_2^* & \mu\gamma_1^*\hat{\nabla}_\xi & -\mu^2 c_g^*\hat{\nabla}_\xi - \rho^2\sigma_2^* + \mu^2 D_1^*\hat{\Delta}_\xi \end{pmatrix}. \tag{22}$$

We recall that $\hat{\nabla}_\xi$ and $\hat{\Delta}_\xi$ are the Fourier symbols of the difference operators ∇ and Δ, respectively, as defined in §1.5.

The eigenvalues, $\Lambda_\xi^{(j)}$ (for $j = 1, 2, 3$), of $\mathrm{M}_\xi(\mu)$ determine the stability of the spatially uniform state (20), where the dependence of $\Lambda_\xi^{(j)}$ on μ is presented in Figure 3. The onset of instability is determined by the eigenvalue (or one of a pair of complex-conjugate eigenvalues) of $\mathrm{M}_\xi(\mu)$ with maximal real part; we denote this eigenvalue as $\Lambda_\xi(\mu)$ for each ξ. At a given value of $\mu > 0$, the perturbed system (21) is neutrally stable if $\mathrm{Re}(\Lambda_\xi(\mu)) \leq 0$ for all ξ, and unstable otherwise. We first note, however, that the rotational and temporal invariance of the spatially uniform state (20) implies that $\Lambda_0 = 0$ has multiplicity two. The remaining eigenvalue for $\xi = 0$ is $-2\mathrm{Re}(\sigma_1) < 0$, corresponding to a stable perturbation from the spatially uniform state for all $\mu > 0$. Hence, if an instability to the spatially uniform state arises, then it is for $\xi > 0$, corresponding to the emergence of a nontrivial spatial pattern.

Numerically we observe that, for any $\xi > 0$, there is an unstable range of μ (for which $\mathrm{Re}(\Lambda_\xi(\mu)) > 0$) of the form $0 < \mu < \mu_\xi$ for some $\mu_\xi > 0$. It follows that the spatially uniform state is stable for $\mu \gtrsim \mu_\xi$. We note that the eigenvalues computed for $\mu \gg 1$ arise in a regime inconsistent with our $\mu = O(1)$ assumption (see §1.5), so we consider only $\mu = O(1)$ when determining the instability threshold, μ_ξ (see Figure 3(a) for reference). In the $\mu = O(1)$ regime of interest, the spatially uniform state is therefore unstable to perturbations for $\mu < \mu_c = \max_\xi \mu_\xi$.

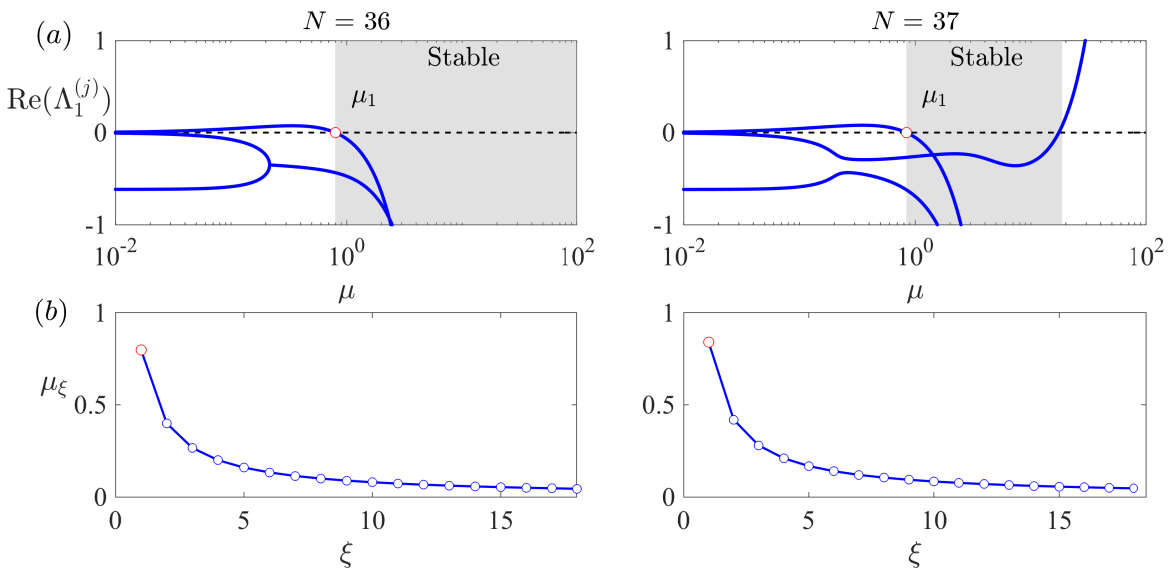

Figure 3: The linear stability of the periodic state for $N = 36$ (left) and $N = 37$ (right). (a) The case $\xi = 1$. The real part of the eigenvalues $\Lambda_1^{(j)}$ for $j = 1, 2, 3$ as a function of μ. The transition from stable (grey shading) to unstable as μ decreases determines the instability threshold for $\xi = 1$ (red circle). For $N = 37$, instability is predicted by the amplitude equations (8) for $\mu \gg 1$, a regime inconsistent with the $\mu = O(1)$ assumption. (b) The instability threshold, μ_ξ, for each integer wavenumber, ξ, for $\xi \leq N/2$. The long-wave mode, $\xi = 1$ (red circle), is the first to destabilize as μ is decreased.

3.2 The onset of spatial amplitude modulations

A crucial feature of the system (8) is the coupling of the complex amplitude, A_n, with the mean, B_n, which acts to drive the instability of the spatially uniform state (20). We observe that variations in B_n act as a source term in the amplitude, A_n, thus promoting spatial variations in A_n. For large μ, the diffusion term in (8a) counteracts the growth of spatial variations of A_n, but this smoothing effect may become subdominant to the source term when μ is sufficiently small. Likewise, a similar competition between diffusion and the excitation of spatial variations in B_n, driven by variations in A_n, is apparent in equation (8b). As a consequence, this coupling provides a positive feedback loop for the emergence of spatial variations, whereas a BFN-like mechanism instead relies on sufficiently small dissipation [52].

In fact, a true BFN instability only arises in the system (8) when the coupling coefficients, γ_i, and the group velocity parameter, c_g, vanish. A necessary condition for instability in this artificial case is $\mathrm{Re}(\sigma_2 D_1^*) < 0$ [21]. By numerically computing the eigenvalues of $\mathrm{M}_\xi(\mu)$, we observe that, similar to the BFN instability, the amplitude equations (8) exhibit a long-wave instability at $\xi = 1$ (see Figure 3(b)); hence, in the cases considered here, we have $\mu_c = \mu_1$. Finally, as discussed in Appendix B, we observe good agreement between the value of μ_c predicted by the linear stability analysis of §3.1 and by direct numerical simulations of the lattice equations (2) for $\alpha \ll 1$, consistent with the validity of our weakly nonlinear theory (see §1.5).

4 Numerical solutions

We now explore the nonlinear dynamics predicted by the amplitude equations (8) beyond the onset of spatial modulations, $\mu < \mu_c$. To proceed, we must select a particular choice for the wave kernel, $\mathcal{H}$. Motivated by the form of the wave field arising in the bouncing-droplet system [32], a candidate wave kernel that satisfies the assumed periodicity, exponential decay and quasi-monochromaticity may be postulated by projecting the form of the dimensionless radially symmetric wave $F(r) = \mathcal{A}\mathrm{J}_0(2\pi r)\mathrm{sech}(r/l)$ onto a circle of circumference $2\pi r_0 = N\delta$, where $r_0 = R/\lambda_W$ [25]. Here J_0 is the Bessel function of the first kind with order zero and $\mathcal{A}$ is the dimensionless amplitude of the wave. The resultant algebraic form of the wave kernel is then taken to be

$$\mathcal{H}(x) = F\left(2r_0 \sin\frac{x}{2r_0}\right), \tag{23}$$

where an example of this wave kernel is given in Figure 2(b). For the numerical results presented herein, we consider $\mathcal{A} = 0.1$ [25]. We note that the qualitative features of these results do not depend on the value of $\mathcal{A}$; increasing $\mathcal{A}$ simply serves to increase the amplitude of the wave field accompanying the equispaced lattice, the main consequence of which is a concomitant decrease in the critical memory, M_c.

As discussed in Appendix C, there is a vast parameter space we could explore with equations (8) by varying the parameters l, δ, and N. We here consider $l = \delta = 2.6$ and explore the effect of decreasing μ below μ_c (equivalently, increasing M) for two adjacent droplet

numbers, $N = 40$ and $N = 41$. These two cases serve to elucidate the key phenomenology exhibited by the amplitude equations (8). A deeper exploration of the parameter space is reserved for future work. Before we present the solutions, we note that the only control parameter in the amplitude equations (8) is μ, since the coefficients are fixed for a particular choice of wave kernel (23) and its constituent parameters, specifically l, δ, and N. Thus, varying μ corresponds to traversing a *particular path through parameter space*, in contrast to varying each coefficient in the amplitude equations independently. As we shall see, this variation in μ gives rise to a series of bifurcations between qualitatively different dynamical behaviors.

The amplitude equations are evolved using a spectral method over the droplet number, n, and a fourth-order Runge-Kutta method in time, for which the linear terms are evolved analytically using an integrating factor (see Appendix D for details) [53]. Initially considering μ just below the instability threshold, $0 < \mu_c - \mu \ll 1$, we evolve the amplitude equations (8) from the initial condition $A_n = \rho + \zeta \sin(n\alpha)$ and $B_n = \zeta \sin(n\alpha)$ with $\zeta = 0.05$ and continue the simulations until a periodic state is attained. Thereafter, we decrement μ by 0.02 and initialize the following simulation at the final values obtained in the preceding simulation. The MATLAB code used to simulate these dynamical states is provided in the Supplementary Material.

In the case of $N = 40$ droplets (see Figure 4), close to the onset of spatial modulations at $\mu = \mu_c$, we first observe a time-independent solution for $|A_n|$ (panel (i)), which destabilizes into a periodic, breather-like state (panel (ii)) with slight dips apparent in $|A_n|$. These dips persist as $\mu_c - \mu$ is increased (panels (iii) and (iv)), but the solution is instead constant in time. We note that when $N = 40$, the group velocity parameter, c_g, is identically zero. For $N = 41$ droplets and $c_g \neq 0$ (Figure 5), similar dynamical transitions occur, although the asymmetry of the system instead yields traveling waves (panel (i)) and propagating states. Notably, we observe parameter regimes for which dark breathers (panel (ii)) and dark solitons (panels (iii)–(v)) arise, characterized by the sharp dips in the amplitude, $|A_n(T)|$, towards zero, features that are not present when $N = 40$. All of the aforementioned features arise over a large range of N, and thus appear to be canonical features of the discrete amplitude equations (8). We also note that the jumps in the bounds of $|A_n|$ and B_n are indicative of

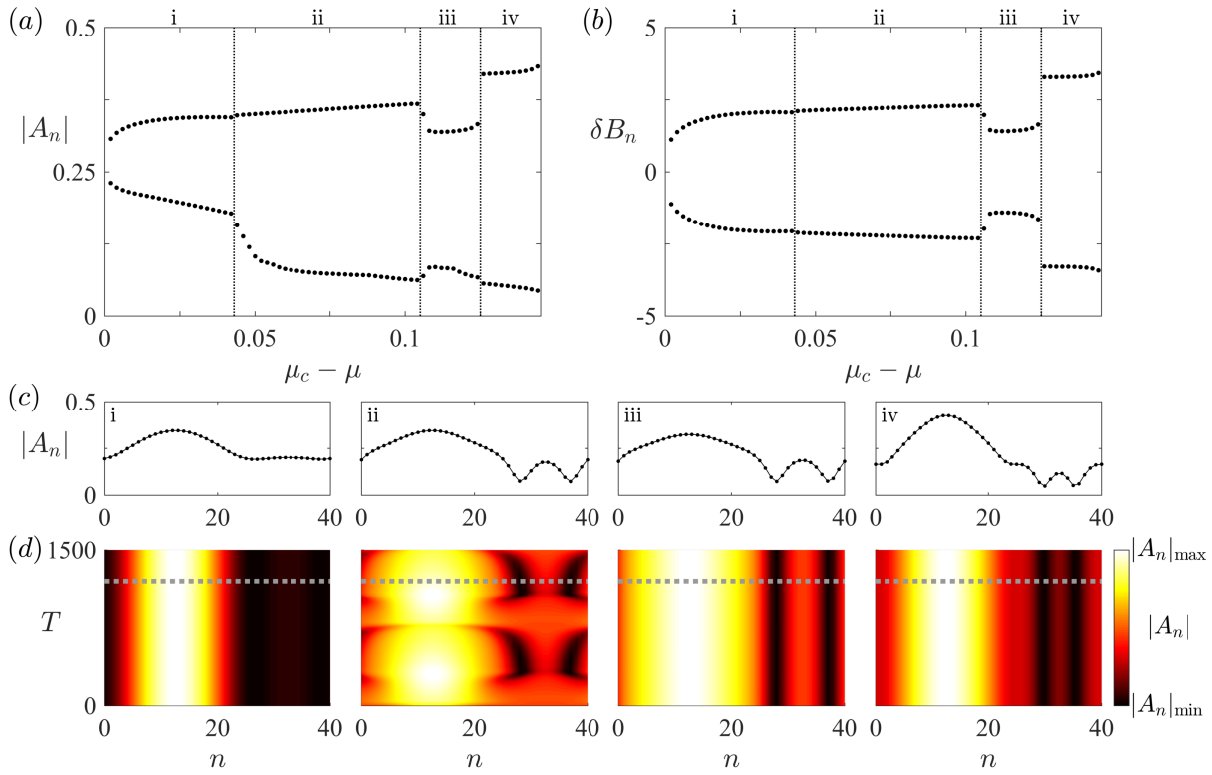

Figure 4: The nonlinear dynamics predicted by the amplitude equations (8) for $N = 40$ droplets and $\mu < \mu_c = 0.852$. The system parameters here are $l = \delta = 2.6$, yielding $k_c = 20$ and $\nu_c = 1.585$. (a) The upper and lower bounds of $|A_n(T)|$ attained over the entire simulation. We identify four dynamical regimes, which are denoted by Roman numerals and divided by the dotted vertical lines. (b) The upper and lower bounds of $\delta B_n(T) = B_n(T) - \langle B_n(T) \rangle$ attained over the entire simulation, where angled brackets denote the average over n. (c) Snapshots of $|A_n|$ at time $T = 1200$ for each dynamical regime, where $\mu_c - \mu$ takes values (i) 0.03, (ii) 0.08, (iii) 0.12, and (iv) 0.14. (d) Corresponding space-time plots of $|A_n(T)|$ for the same parameter values as (c). The dashed lines correspond to the snapshot time, $T = 1200$.

hysteresis between dynamical states, an effect to be explored in greater detail elsewhere.

Finally, we recall that the difference operators, ∇ and Δ, are derived systematically from the DFT. In Appendix E, we consider the dynamics predicted by the amplitude equations (8) when the difference operators are instead replaced by local central finite difference operators. A stencil of $2p + 1$ points therefore gives rise to explicit interaction of a particular droplet with its p-nearest neighbors. We generally observe qualitatively similar dynamics arising for $p = 1$, with apparent convergence to the results computed with the DFT difference operators as p is successively increased. However, one surprising feature is the emergence of stable bright solitons for $p = 1$, a feature not apparent for $p > 1$ or for the DFT difference operators. We conclude, therefore, that the dynamics predicted by the amplitude equations (8) may change profoundly if one considers different couplings between droplets, an effect to be explored in greater detail elsewhere.

5 Discussion and conclusion

In this paper, we have presented a rigorous mathematical framework to derive a discrete and periodic set of amplitude equations from a driven and dissipative oscillator model, inspired by the physics of droplet lattices bouncing on a vibrating fluid bath [24]. Our systematic derivation provides a direct link between the constitutive properties of the lattice model (2) (specifically, the wave kernel, $\mathcal{H}$) and the coefficients arising in the amplitude equations (8). A linear stability analysis of the amplitude equations (8) reveals the importance of the coupling to the discrete mean equation (8b) in destabilizing the system from a spatially uniform state, leading to spatial modulations in the droplet oscillation amplitude following a second bifurcation, similar in spirit to the BFN instability.

Beyond this second bifurcation, numerical solutions of the amplitude equations (8) reveal a fascinating family of dynamical behaviors including dark solitons, breather states, and traveling waves. It remains an open question as to whether such states are robust when considering the continuous analogue of the amplitude equations (8) [54, 55, 56]. As computational models of the droplet system advance [57], the predictions of the amplitude equations may be compared against direct numerical simulations of the droplet dynamics, paving the

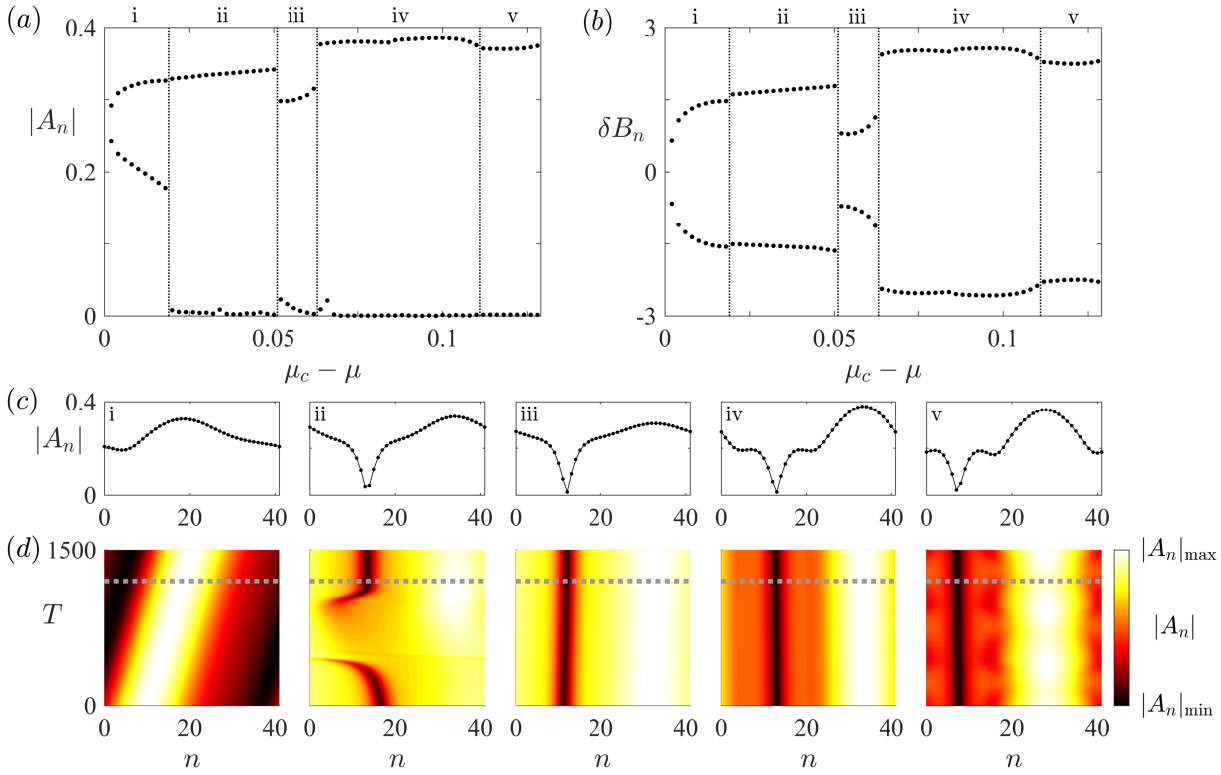

Figure 5: The nonlinear dynamics predicted by the amplitude equations (8) for $N = 41$ droplets and $\mu < \mu_c = 0.853$. The system parameters here are $l = \delta = 2.6$, yielding $k_c = 20$ and $\nu_c = 1.582$. (a) The upper and lower bounds of $|A_n(T)|$ attained over the entire simulation. We identify five dynamical regimes, which are denoted by Roman numerals and divided by the dotted vertical lines. (b) The upper and lower bounds of $\delta B_n(T) = B_n(T) - \langle B_n(T) \rangle$ attained over the entire simulation, where angled brackets denote the average over n. (c) Snapshots of $|A_n|$ at time $T = 1200$ for each dynamical regime, where $\mu_c - \mu$ takes values (i) 0.014, (ii) 0.046, (iii) 0.06, (iv) 0.08, and (v) 0.1. (d) Corresponding spacetime plots of $|A_n(T)|$ for the same parameter values in (c). The dashed lines correspond to the snapshot time, $T = 1200$.

way for further experimental investigation [24]. In particular, a tantalizing prospect is to hunt for the emergence of so-called chimera states [58, 59], thought to be ubiquitous in coupled oscillators subject to non-local coupling, but have been shown to exist in only a handful of experimental systems to date [60, 61, 62, 63].

We conclude with the proposition that the framework used to derive the amplitude equations (8) applies to a more general class of periodic oscillator models of canonical form

$$\ddot{x}_n + \dot{x}_n = -\frac{\partial h}{\partial x}(x_n, t), \tag{24a}$$

$$\mathcal{P}h = \sum_{m=1}^{N} \mathcal{H}(x - x_m), \tag{24b}$$

with the linear operator $\mathcal{P} = \partial/\partial t + \nu$ in equation (2b) serving as a particular example. The novelty of the model (24) is that the inter-particle coupling potential, h, is *dynamic*, continuously evolving with the particle motion, rather than being fixed in space or with respect to the particles. Other potential choices of $\mathcal{P}$ are numerous, and could lead to an even richer family of dynamics. For a particular choice of $\mathcal{P}$, if the bifurcation leading to instability of the oscillator is of supercritical Andronov-Hopf type, then one should expect a complex Ginzburg-Landau equation in the vicinity of the bifurcation point. However, the precise form of the amplitude equations will change depending on the type of primary bifurcation that arises and the inherent symmetries of the system [5, 7]. Such an investigation may lead to further theoretical insights into the dynamics and pattern-forming behavior of active particles in complex environments [35, 64].

Acknowledgments

The authors would like to thank the anonymous referees whose comments led to the improvement of this article. R. R. R. gratefully acknowledges the NSF for financial support through Grant No. DMS-1719637.

Appendix A Derivation of the Ginzburg-Landau and mean equations

Further details are here provided of the multiple-scales expansion leading to the complex Ginzburg-Landau and mean equations (8). The general procedure toward obtaining equations (8) is to substitute the asymptotic expansions (10) into the lattice equations (2) and gather successive powers of ε. At each successive order, we suppress resonant terms proportional to $\mathrm{e}^{\mathrm{i}\phi_n(t)}$ (where $\phi_n(t) = k_c n\alpha + \omega_c t$) or those constant in t. To extract all relevant terms at each order, we must introduce auxiliary variables to solve for the free surface (see §2.1), expand convolutions in the manner summarized in §2.2, and consider the limit of weak asymmetry (§2.3). For notational efficiency, we denote $\mathcal{H}_m = \mathcal{H}(m\delta)$, $\mathcal{H}'_m = \mathcal{H}'(m\delta)$, and so forth.

At leading order we obtain

$$\left.\frac{\partial h^{(0)}}{\partial x}\right|_{x=n\delta} = 0, \quad h^{(0)}(x) = \frac{1}{\nu_c}\sum_{m=1}^{N}\mathcal{H}(x-m\delta), \tag{25}$$

reflecting the fact that the free-surface gradient beneath each droplet vanishes in the steady-state. It may be readily verified that all odd-derivatives of $h^{(0)}$ vanish beneath each droplet at equilibrium, a fact we will make repeated use of in simplifying the forthcoming terms arising in our expansion.

The problem at $O(\varepsilon)$ has already been discussed in §2 and thus we proceed directly to $O(\varepsilon^2)$, remembering that terms from the right-hand side of equation (19) are promoted to $O(\varepsilon^3)$ after setting $\alpha = \mu\varepsilon$. The lattice equations at $O(\varepsilon^2)$ are

$$\frac{\partial^2 x_n^{(2)}}{\partial t^2} + \frac{\partial x_n^{(2)}}{\partial t} = -\left\{\frac{\partial h^{(2)}}{\partial x} + x_n^{(2)}\frac{\partial^2 h^{(0)}}{\partial x^2} + x_n^{(1)}\frac{\partial^2 h^{(1)}}{\partial x^2}\right\}\Big|_{x=n\delta}, \tag{26}$$

$$\frac{\partial h^{(2)}}{\partial t} + \nu_c h^{(2)} = h^{(0)} + \sum_{m=1}^{N}\left\{\frac{1}{2}\big(x_m^{(1)}\big)^2\mathcal{H}''(x-m\delta) - x_m^{(2)}\mathcal{H}'(x-m\delta)\right\}. \tag{27}$$

Following the procedure outlined in §2.1, we solve for $h^{(2)}$ by introducing two further auxiliary variables, Y_n and Z_n, satisfying

$$\frac{\partial Y_n}{\partial t} + \nu_c Y_n = \frac{1}{2}\big(x_n^{(1)}\big)^2, \qquad \frac{\partial Z_n}{\partial t} + \nu_c Z_n = x_n^{(2)}, \tag{28}$$

chosen to match the coefficients of the wave kernel on the right-hand side of (27). Hence, a particular solution of (27) is

$$h^{(2)} = \frac{1}{\nu_c} h^{(0)} + \sum_{m=1}^{N} \left\{ Y_m \mathcal{H}''(x - m\delta) - Z_m \mathcal{H}'(x - m\delta) \right\}. \tag{29}$$

By substituting the form of $x_n^{(1)}$, given by equation (15), into the first equation of (28), we obtain the particular solution

$$Y_n = \frac{1}{\nu_c} \left[|A_n|^2 + \frac{1}{2} B_n^2 \right] + B_n \left[\frac{A_n}{\nu_c + \mathrm{i}\omega_c} \mathrm{e}^{\mathrm{i}\phi_n} + \text{c.c.} \right] + \frac{1}{2} \left[\frac{A_n^2}{\nu_c + 2\mathrm{i}\omega_c} \mathrm{e}^{2\mathrm{i}\phi_n} + \text{c.c.} \right]. \tag{30}$$

Substituting (29) and (30) into (26), and then using (25), yields

$$\begin{aligned} \mathcal{L}_n \boldsymbol{x}^{(2)} = {} & \left[B_n + \{ A_n \mathrm{e}^{\mathrm{i}\phi_n} + \text{c.c.} \} \right] \left[\frac{1}{\nu_c} \sum_{m=1}^{N} B_{n-m} \mathcal{H}_m''' + \left\{ \mathrm{e}^{\mathrm{i}\phi_n} \sum_{m=1}^{N} \frac{A_{n-m} \mathrm{e}^{-\mathrm{i}k_c m\alpha}}{\nu_c + \mathrm{i}\omega_c} \mathcal{H}_m''' + \text{c.c.} \right\} \right] \\ & - \frac{1}{\nu_c} \sum_{m=1}^{N} \left[\frac{1}{2} B_{n-m}^2 + |A_{n-m}|^2 \right] \mathcal{H}_m''' - \left[\mathrm{e}^{\mathrm{i}\phi_n} \sum_{m=1}^{N} \frac{A_{n-m} B_{n-m}}{\nu_c + \mathrm{i}\omega_c} \mathrm{e}^{-\mathrm{i}k_c m\alpha} \mathcal{H}_m''' + \text{c.c.} \right] \\ & - \frac{1}{2} \left[\mathrm{e}^{2\mathrm{i}\phi_n} \sum_{m=1}^{N} \frac{A_{n-m}^2 \mathrm{e}^{-2\mathrm{i}k_c m\alpha} \mathcal{H}_m'''}{\nu_c + 2\mathrm{i}\omega_c} + \text{c.c.} \right]. \end{aligned} \tag{31}$$

Analogous to §2.2, we now use the asymptotic expansion (18) to express convolutions on the right-hand side of (31) in powers of α. After some arduous algebra, we reduce (31) to the highly simplified form

$$\begin{aligned} \mathcal{L}_n \boldsymbol{x}^{(2)} = {} & 2\mathrm{Re}\left[\sum_{m=1}^{N} \frac{\mathrm{e}^{-\mathrm{i}k_c m\alpha} \mathcal{H}_m'''}{\nu_c + \mathrm{i}\omega_c} \right] |A_n|^2 + \alpha \left[\hat{\gamma}_1 \mathrm{e}^{\mathrm{i}\phi_n} A_n \nabla B_n + \text{c.c.} \right] + 2\alpha \mathrm{Re}\left[\hat{\gamma}_2 A_n \nabla A_n^* \right] \\ & + \left[\hat{c}_1 A_n^2 \mathrm{e}^{2\mathrm{i}\phi_n} + \text{c.c.} \right] + \alpha \left[\hat{c}_2 \mathrm{e}^{2\mathrm{i}\phi_n} A_n \nabla A_n + \text{c.c.} \right] + O(\alpha^2), \end{aligned} \tag{32}$$

where the complex coefficients are defined as

$$\begin{aligned} \hat{\gamma}_1 &= \sum_{m=1}^{N} \left(\frac{\mathrm{e}^{-\mathrm{i}k_c m\alpha}}{\nu_c + \mathrm{i}\omega_c} - \frac{1}{\nu_c} \right) a_m \mathcal{H}_m''', \qquad \hat{\gamma}_2 = \sum_{m=1}^{N} \left(\frac{1}{\nu_c} - \frac{\mathrm{e}^{\mathrm{i}k_c m\alpha}}{\nu_c - \mathrm{i}\omega_c} \right) a_m \mathcal{H}_m''', \\ \hat{c}_1 &= \sum_{m=1}^{N} \left[\frac{\mathrm{e}^{-\mathrm{i}k_c m\alpha}}{\nu_c + \mathrm{i}\omega_c} - \frac{\mathrm{e}^{-2\mathrm{i}k_c m\alpha}}{2(\nu_c + 2\mathrm{i}\omega_c)} \right] \mathcal{H}_m''', \quad \hat{c}_2 = \sum_{m=1}^{N} \left(\frac{\mathrm{e}^{-2\mathrm{i}k_c m\alpha}}{\nu_c + 2\mathrm{i}\omega_c} - \frac{\mathrm{e}^{-\mathrm{i}k_c m\alpha}}{\nu_c + \mathrm{i}\omega_c} \right) a_m \mathcal{H}_m'''. \end{aligned} \tag{33}$$

To apply the weak-asymmetry approximation developed in §2.3 to the coefficient of $|A_n|^2$ on the right-hand side of equation (32), we first note that

$$2\mathrm{Re}\left[\sum_{m=1}^{N} \frac{\mathrm{e}^{-\mathrm{i}k_c m\alpha} \mathcal{H}_m'''}{\nu_c + \mathrm{i}\omega_c} \right] = 2\mathrm{Re}\left[\frac{\mathrm{i}}{\nu_c + \mathrm{i}\omega_c} \right] \sum_{m=1}^{N} (-1)^m \sin(m\alpha\chi) \mathcal{H}_m''',$$

where $\chi = N/2 - k_c$. By a similar argument to which the group velocity was promoted to $O(\varepsilon^3)$ in §2.3, the coefficient of $|A_n|^2$ has size $O(\alpha)$ for $\alpha \ll 1$ and $\chi = O(1)$, so the corresponding term in (32) should likewise appear at $O(\varepsilon^3)$. We thus write

$$2\mathrm{Re}\left[\sum_{m=1}^{N} \frac{\mathrm{e}^{-\mathrm{i}k_c m\alpha}\mathcal{H}_m'''}{\nu_c + \mathrm{i}\omega_c}\right]|A_n|^2 = \alpha\hat{\gamma}_3|A_n|^2,$$

where the $O(1)$ real coefficient $\hat{\gamma}_3$ is defined as

$$\hat{\gamma}_3 = \frac{2}{\alpha}\mathrm{Re}\left[\sum_{m=1}^{N} \frac{\mathrm{e}^{-\mathrm{i}k_c m\alpha}\mathcal{H}_m'''}{\nu_c + \mathrm{i}\omega_c}\right]. \tag{34}$$

In a similar spirit, we deduce that the coefficient $\hat{c}_1$ is size $O(\alpha)$ when $\chi > 0$ and zero otherwise. Therefore the non-secular terms in (32) (those that are proportional to $\mathrm{e}^{2\mathrm{i}\phi_n}$) are both of size $O(\alpha)$ and so should actually appear at $O(\varepsilon^3)$. However, as these terms will still be non-secular at that order, they play no role in the derived amplitude equations for A_n and B_n. We conclude that all the inhomogeneities in (32) (each of which is of size $O(\alpha)$) should instead appear at $O(\varepsilon^3)$. Hence, at $O(\varepsilon^2)$, we have $\mathcal{L}_n\boldsymbol{x}^{(2)} = 0$, which is identical to the problem for $\boldsymbol{x}^{(1)}$. Akin to the solution *ansatz* at $O(\varepsilon)$, we therefore pose

$$x_n^{(2)} = E_n(T) + \left[C_n(T)\mathrm{e}^{\mathrm{i}\phi_n} + \mathrm{c.c.}\right], \quad Z_n = \frac{1}{\nu_c}E_n(T) + \left[\frac{C_n(T)}{\nu_c + \mathrm{i}\omega_c}\mathrm{e}^{\mathrm{i}\phi_n} + \mathrm{c.c.}\right],$$

which, when applying the asymptotic expansion of the convolution (see §2.2), satisfies the inhomogeneous problem to leading order. The $O(\alpha^2)$ terms that arise out of the expansion of this convolution appear at $O(\varepsilon^4)$, which is beyond the order presented in this calculation.

At $O(\varepsilon^3)$, the lattice equations (2) yield a system for $x_n^{(3)}$ and $h^{(3)}$, namely

$$\begin{aligned}\frac{\partial^2 x_n^{(3)}}{\partial t^2} + \frac{\partial x_n^{(3)}}{\partial t} + x_n^{(3)}\frac{\partial^2 h^{(0)}}{\partial x^2}\bigg|_{x=n\delta} &= -\left[2\frac{\partial^2 x_n^{(1)}}{\partial t\partial T} + \frac{\partial x_n^{(1)}}{\partial T}\right] \\ &\quad -\left[\frac{\partial h^{(3)}}{\partial x} + x_n^{(1)}\frac{\partial^2 h^{(2)}}{\partial x^2} + \frac{1}{2}\big(x_n^{(1)}\big)^2\frac{\partial^3 h^{(1)}}{\partial x^3} + x_n^{(2)}\frac{\partial^2 h^{(1)}}{\partial x^2} + \frac{1}{6}\big(x_n^{(1)}\big)^3\frac{\partial^4 h^{(0)}}{\partial x^4}\right]\bigg|_{x=n\delta}\end{aligned} \tag{35}$$

and

$$\begin{aligned}\frac{\partial h^{(3)}}{\partial t} + \nu_c h^{(3)} &= -\left[\frac{\partial h^{(1)}}{\partial T} - h^{(1)}\right] \\ &\quad + \sum_{m=1}^{N}\left\{x_m^{(1)}x_m^{(2)}\mathcal{H}''(x - m\delta) - x_m^{(3)}\mathcal{H}'(x - m\delta) - \frac{1}{6}\big(x_m^{(1)}\big)^3\mathcal{H}'''(x - m\delta)\right\}.\end{aligned} \tag{36}$$

Appended to the right-hand side of (35) will be the terms promoted from both $O(\varepsilon)$ and $O(\varepsilon^2)$. We follow an identical procedure to our analysis at $O(\varepsilon)$ and $O(\varepsilon^2)$. First we introduce three auxiliary variables (§2.1), one for each of the three inhomogeneities in curly brackets on the right-hand side of equation (36), and then solve for $h^{(3)}$. We then substitute this solution into (35), along with the droplet positions and wave field terms computed from lower orders, and then apply the slowly varying approximation (§2.2) to reduce discrete convolutions to an asymptotic expansion in powers of α. This procedure gives rise to a system of the form $\mathcal{L}_n \boldsymbol{x}^{(3)} = \text{RHS}$, where the right-hand side (RHS) is composed of terms that are constant in t, terms with coefficients $\mathrm{e}^{\pm \mathrm{i}\phi_n(t)}$, and non-secular terms (whose form can be ignored at this stage). For a bounded solution, we require that the constant and $\mathrm{e}^{\mathrm{i}\phi_n}$ secular terms have vanishing coefficients, which yields the following evolution equations for the complex amplitude, A_n, and the real drift, B_n:

$$\hat{\sigma}_0 \frac{\mathrm{d}A_n}{\mathrm{d}T} + \mu^2 \hat{c}_g \nabla A_n = \hat{\sigma}_1 A_n - \hat{\sigma}_2 |A_n|^2 A_n + \mu \hat{\gamma}_1 A_n \nabla B_n + \mu^2 \hat{D}_1 \Delta A_n, \tag{37a}$$

$$\hat{b}_0 \frac{\mathrm{d}B_n}{\mathrm{d}T} = \mu^2 \hat{D}_2 \Delta B_n + 2\mu \mathrm{Re}\big[\hat{\gamma}_2 A_n \nabla A_n^*\big] + \mu \hat{\gamma}_3 |A_n|^2, \tag{37b}$$

where $\mu = \alpha/\varepsilon$ and we have neglected terms whose coefficients are of size $O(\alpha)$ at $O(\varepsilon^3)$ (§2.3). We note that we cannot determine the higher-order corrections (C_n and E_n) without proceeding to $O(\varepsilon^4)$ and higher. However, a satisfactory approximation is obtained by considering A_n and B_n alone, which form a closed system.

Recalling that $\mathcal{D}_k(\lambda;\nu)$ is the dispersion relation (4), the coefficients (other than the $\hat{\gamma}_i$ defined in equations (33) and (34)) appearing in (37a) are as follows:

$$\hat{\sigma}_0 = \frac{\partial \mathcal{D}_{k_c}}{\partial \lambda}(\mathrm{i}\omega_c;\nu_c), \quad \hat{\sigma}_1 = \frac{\partial \mathcal{D}_{k_c}}{\partial \nu}(\mathrm{i}\omega_c;\nu_c),$$

$$\hat{\sigma}_2 = \frac{3}{2\nu_c}\sum_{m=1}^{N} \mathcal{H}_m'''' - \sum_{m=1}^{N} \mathcal{H}_m'''' \mathrm{Re}\left[\frac{\mathrm{e}^{-\mathrm{i}k_c m\alpha}}{\nu_c + \mathrm{i}\omega_c}\right] + \frac{1}{2}\sum_{m=1}^{N} \frac{\mathrm{e}^{-2\mathrm{i}k_c m\alpha}\mathcal{H}_m''''}{\nu_c + 2\mathrm{i}\omega_c} - \sum_{m=1}^{N} \frac{\mathcal{H}_m'''' \mathrm{e}^{-\mathrm{i}k_c m\alpha}}{\nu_c + \mathrm{i}\omega_c},$$

$$\hat{D}_1 = \frac{1}{\nu_c + \mathrm{i}\omega_c}\sum_{m=1}^{N} b_m \mathrm{e}^{-\mathrm{i}k_c m\alpha}\mathcal{H}_m'',$$

while those that appear in (37b) are

$$\hat{b}_0 = \frac{\partial \mathcal{D}_0}{\partial \lambda}(0;\nu_c) = 1 + \frac{1}{\nu_c^2}\sum_{m=1}^{N} \mathcal{H}_m'', \qquad \hat{D}_2 = \frac{1}{\nu_c}\sum_{m=1}^{N} b_m \mathcal{H}_m''.$$

Upon dividing (37a) by $\hat{\sigma}_0$ and (37b) by $\hat{b}_0$, we arrive at equations (8), where $(c_g, \sigma_1, \sigma_2, \gamma_1, D_1) = (\hat{c}_g, \hat{\sigma}_1, \hat{\sigma}_2, \hat{\gamma}_1, \hat{D}_1)/\hat{\sigma}_0$ and $(D_2, \gamma_2, \gamma_3) = (\hat{D}_2, \hat{\gamma}_2, \hat{\gamma}_3)/\hat{b}_0$.

Appendix B The onset of spatial modulations

We here consider the predicted value of the instability threshold, μ_c, at which the periodic lattice destabilizes and spatial modulations emerge ($\mu < \mu_c$). We compare the values of μ_c obtained by directly simulating the lattice equations (2), and those computed using the linear stability analysis of the derived amplitude equations in §3. The lattice equations are simulated using the spectral code presented in [25]. We initialized the system with $\mu > \mu_c$ (for which the spatially uniform state is stable) and successively decremented μ, starting each simulation from the final values of the system variables (x_n, $\dot{x}_n$, h) attained with the previous value of μ. The value of μ_c was then estimated by the threshold at which spatial modulations emerged in our simulations, with a typical error estimated to be ± 0.01.

The results of this study are presented in Table 2 for $\mathcal{A} = 0.1$, $\delta = 1.6$ and $l = 1.6$. As the number of droplets, N, is increased, the agreement between the numerical (lattice simulations) and theoretical (linear stability analysis) results improves, consistent with the validity of our weakly nonlinear theory, $\alpha = 2\pi/N \ll 1$. Similar convergence between theory and simulations was also verified for N odd.

N	30	40	50	60	70
Num. (± 0.01)	1.28	1.16	1.15	1.19	1.21
Theor.	0.85	0.98	1.10	1.18	1.23
$\alpha = 2\pi/N$	0.21	0.16	0.13	0.10	0.09

Table 2: Comparison between the numerical (Num.) and theoretical (Theor.) predictions of the instability threshold, μ_c, computed with the difference operators, ∇ and Δ, derived from the DFT.

Appendix C Dependence of μ_c on changes to the wave field and lattice parameters

In this section, we explore the dependence of μ_c on the inter-droplet spacing, δ, and spatial decay length, l, of the wave kernel, $\mathcal{H}$, defined by equation (23). As presented in Figure 6, the dependence of the onset of spatial modulations on the system parameters, l and δ, can be quite intricate. Near the boundaries between super- and sub-critical Andronov-Hopf bifurcations (where geometric and subcritical Andronov-Hopf instabilities arise in the white regions in Figure 6), μ_c can be very large—a feature that appears to be correlated with k_c departing from $N/2$—inconsistent with the $\mu = O(1)$ assumption under which the amplitude equations (8) were derived. Away from these boundaries, we observe regions in which $\mu_c = O(1)$; indeed, simulation of the lattice system (2) reveals favorable agreement of the numerical and theoretical instability threshold. (This agreement improves as $\alpha = 2\pi/N$ becomes smaller, consistent with our assumptions; see Appendix B.) Near the middle of each 'band' in which supercritical Andronov-Hopf bifurcations arise, we observe that $\mu_c = 0$, corresponding to the prediction of unconditional stability of the spatially uniform solution (20). Finally, we remark that $\mu_c = O(1)$ is most apparent for $l \sim \delta$, a regime consistent with the validity of our asymptotic expansion of convolutions (see §2.2).

Appendix D Numerical implementation

To evolve the amplitude equations (8), we apply the DFT, $\mathscr{F}_\xi$, to each equation, and then introduce an integrating factor to integrate the linear components exactly [53]. Specifically, we denote $\hat{A}_\xi = \mathscr{F}_\xi[A_n]$ and $\hat{B}_\xi = \mathscr{F}_\xi[B_n]$ for $\xi = 0, \ldots, N-1$ (see equation (9a) for details). By applying the DFT to the amplitude equations (8), we obtain

$$\frac{\mathrm{d}\hat{A}_\xi}{\mathrm{d}T} + \mathcal{M}_\xi \hat{A}_k = \mathscr{F}_\xi\big[\mu\gamma_1 A_n \nabla B_n - \sigma_2 |A_n|^2 A_n\big], \tag{38a}$$

$$\frac{\mathrm{d}\hat{B}_\xi}{\mathrm{d}T} + \mathcal{N}_\xi \hat{B}_\xi = \mathscr{F}_\xi\big[2\mu \mathrm{Re}\left[\gamma_2 A_n \nabla A_n^*\right] + \mu\gamma_3 |A_n|^2\big], \tag{38b}$$

where

$$\mathcal{M}_\xi = \mu^2 c_g \hat{\nabla}_\xi - \sigma_1 - \mu^2 D_1 \hat{\Delta}_\xi \quad \text{and} \quad \mathcal{N}_\xi = -\mu^2 D_2 \hat{\Delta}_\xi.$$

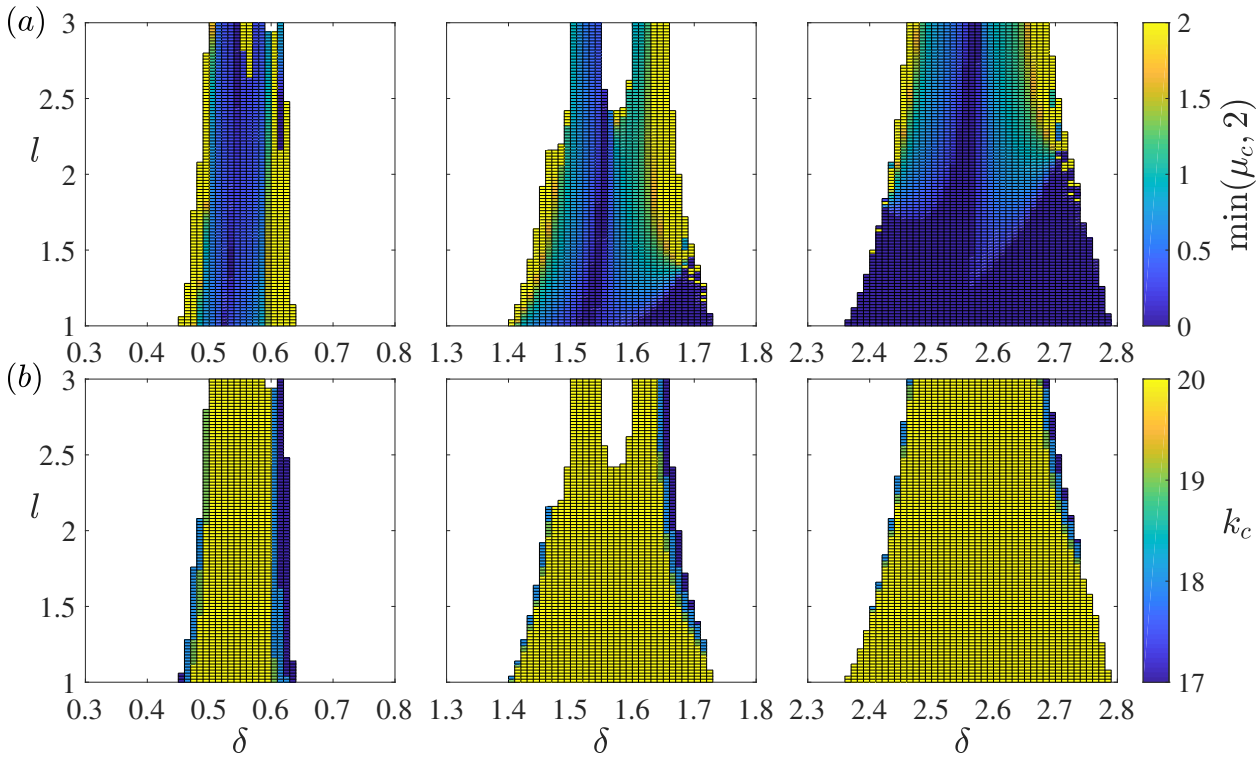

Figure 6: The onset of spatial modulations for $N = 40$ droplets, as predicted by the linear stability analysis of the amplitude equations (8) (see §3) for the wave kernel defined in equation (23). (a) When the initial instability of the equidistant lattice arises *via* a supercritical Andronov-Hopf bifurcation, we color-code each value of the spacing parameter, δ, and the decay length, l, by $\min(\mu_c, 2)$, where spatial instabilities arise for $\mu < \mu_c$. Our theory is valid when $\mu_c = O(1)$. When $\mu_c = 0$, the periodic state is predicted to be unconditionally stable. Large values of μ_c (i.e. those exceeding the plotting threshold of 2) arise near the boundary between super- and sub-critical Andronov-Hopf bifurcations. (b) The corresponding value of k_c, as predicted by the linear stability analysis summarized in §1.3, demonstrating the correlation between large μ_c and $k_c < N/2$.

We recall that $\hat{\nabla}_\xi$ and $\hat{\Delta}_\xi$ are the Fourier symbols of the difference operators ∇ and Δ, respectively (see §1.5). To account for the stiffness manifest in the operators $\mathcal{M}_\xi$ and $\mathcal{N}_\xi$, we introduce an integrating factor. When evolving from time $T = T_n$ to $T = T_{n+1}$, we recast

(38) as

$$\frac{\mathrm{d}}{\mathrm{d}T}\big(\hat{A}_\xi \mathrm{e}^{\mathcal{M}_\xi(T-T_n)}\big) = \mathscr{F}_\xi\big[\mu\gamma_1 A_n \nabla B_n - \sigma_2 |A_n|^2 A_n\big]\mathrm{e}^{\mathcal{M}_\xi(T-T_n)}, \tag{39a}$$

$$\frac{\mathrm{d}}{\mathrm{d}T}\big(\hat{B}_\xi \mathrm{e}^{\mathcal{N}_\xi(T-T_n)}\big) = \mathscr{F}_\xi\big[2\mu\mathrm{Re}\left[\gamma_2 A_n \nabla A_n^*\right] + \mu\gamma_3 |A_n|^2\big]\mathrm{e}^{\mathcal{N}_\xi(T-T_n)}, \tag{39b}$$

and then evolve the variables $\hat{A}_\xi \mathrm{e}^{\mathcal{M}_\xi(T-T_n)}$ and $\hat{B}_\xi \mathrm{e}^{\mathcal{N}_\xi(T-T_n)}$ using a fourth-order Runge-Kutta method. For the numerical results presented in §4, we consider the fixed time step $T_{n+1} - T_n = 0.02$. MATLAB code implementing this numerical scheme is provided in the Supplementary Material.

Appendix E Alternative difference stencils

We consider here how the dynamics predicted by the amplitude equations (8) depend on the form of the difference operators, ∇ and Δ. In §2.2, we derived ∇ and Δ using the discrete Fourier transform (DFT); here we consider the dynamics arising when ∇ and Δ are replaced with symmetric first- and second-order finite difference stencils for p-nearest neighbors (see §E.2).

E.1 Dependence on the number of nearest neighbors

In the following series of tests, we define the wave kernel using $l = 2.6$, $\delta = 2.6$ and $\mathcal{A} = 0.1$ (see §4). We then fix the distance from the onset of spatial modulations (the BFN-like instability), $\mu_c - \mu$, and simulate the system until a periodic state is obtained. In all cases considered, we initialize from a small perturbation about the spatially uniform state (see §3.1), namely $A_n(0) = \rho + 0.05\sin(\alpha n)$ and $B_n(0) = 0.05\sin(\alpha n)$. Finally, we measure characteristic properties of the long-time dynamics, comparing the measured values for different values of p and the difference operators derived from the DFT.

In Figure 7, we present the dynamics of a dark breather arising for $N = 40$ droplets with $\mu_c - \mu = 0.08$. We here characterize the dynamics in terms of the breather period, P_p. We note that the change in the period is much smaller when p is increased from 2 to 3, as compared to when p is increased from 1 to 2. In particular, we observe that P_p approaches the period, P_{DFT}, computed using the DFT difference operators.

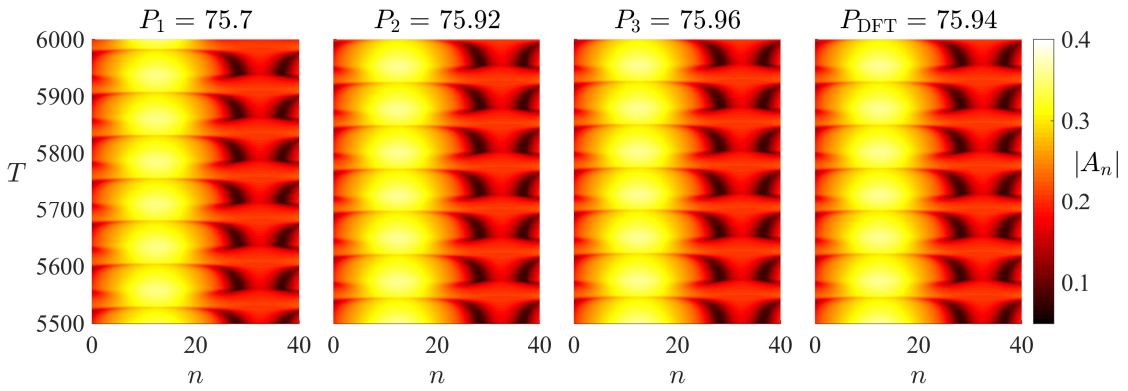

Figure 7: Evolution of the complex amplitude, $|A_n(T)|$, over the slow time scale, T, for a dark breather arising for $N = 40$ droplets with $\mu_c - \mu = 0.08$. We compute the period, P_p, for p-nearest neighbors and compare the results to the period, P_{DFT}, computed using the difference operators derived from the DFT. The corresponding parameter values are listed in §E.1. The differences between P_2, P_3 and P_{DFT} are on the order of the numerical time step, 0.02, forming a lower bound for the precision of the computation of the period.

Likewise, in Figure 8, we present the dynamics of a dark soliton arising for $N = 41$ droplets with $\mu_c - \mu = 0.06$. Specifically, we measure the asymptotic wave speed, C_p, defined as the reciprocal of the time between which the integer $\mathrm{argmin}_n |A_n(T)|$ changes. In other words, when taking an integer to be the unit of length, the slope apparent in each panel of Figure 8 is $1/C_p$. We note that the wave speed approximately halves as p is increased from 1 to 2, but is almost identical for p equal to 2 or 3. Again, C_p approaches the speed, C_{DFT}, computed for the difference operators derived using the DFT.

Finally, we note that μ_c also depends weakly on p, as is evident from the linear stability analysis outlined in §3.1. For the case of $N = 40$ droplets with the foregoing parameters, we compute the following values: $\mu_c = 0.85066$ for $p = 1$; $\mu_c = 0.85179$ for $p = 2$; $\mu_c = 0.85180$ for $p = 3$; and $\mu_c = 0.85180$ for the DFT difference operators. For the case of $N = 41$ droplets, we likewise compute: $\mu_c = 0.85153$ for $p = 1$; $\mu_c = 0.85279$ for $p = 2$; $\mu_c = 0.85280$ for $p = 3$; and $\mu_c = 0.85280$ for the DFT difference operators. In both cases, we observe convergence in the value of μ_c as p is increased, towards that computed using the DFT difference operators.

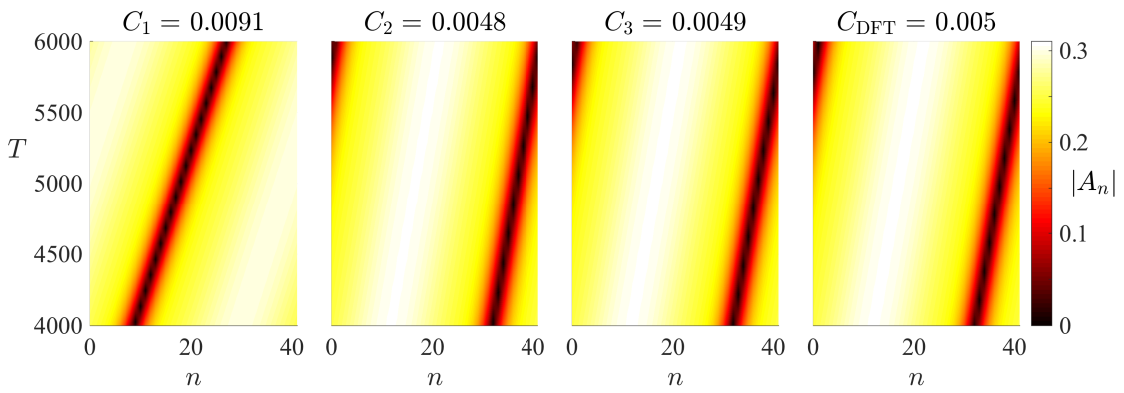

Figure 8: Evolution of the complex amplitude, $|A_n(T)|$, over the slow time scale, T, for a dark soliton arising for $N = 41$ droplets with $\mu_c - \mu = 0.06$. We compute the wave speed, C_p, for p-nearest neighbors and compare the results to the wave speed, C_{DFT}, computed using the difference operators derived from the DFT. The corresponding parameter values are listed in §E.1.

E.2 Finite difference stencils

For a sequence, F_n, with $F_n = F_{n+N}$ and $\alpha = 2\pi/N$, we proceed to define the difference operators, ∇ and Δ, for p-nearest neighbor interactions, and the respective Fourier symbols, $\hat{\nabla}_\xi$ and $\hat{\Delta}_\xi$.

For $p = 1$, we define

$$\nabla F_n = \frac{1}{2\alpha}\Big(F_{n+1} - F_{n-1}\Big)$$

and

$$\Delta F_n = \frac{1}{\alpha^2}\Big(F_{n+1} - 2F_n + F_{n-1}\Big).$$

The corresponding Fourier symbols are

$$\hat{\nabla}_\xi = \frac{\mathrm{i}\sin(\xi\alpha)}{\alpha}$$

and

$$\hat{\Delta}_\xi = \frac{2(\cos(\xi\alpha) - 1)}{\alpha^2},$$

respectively.

For $p = 2$, we define

$$\nabla F_n = \frac{1}{\alpha}\left(\frac{1}{12}F_{n-2} - \frac{2}{3}F_{n-1} + \frac{2}{3}F_{n+1} - \frac{1}{12}F_{n+2}\right)$$

and

$$\Delta F_n = \frac{1}{\alpha^2}\bigg(-\frac{1}{12}F_{n-2} + \frac{4}{3}F_{n-1} - \frac{5}{2}F_n + \frac{4}{3}F_{n+1} - \frac{1}{12}F_{n+2}\bigg).$$

The corresponding Fourier symbols are

$$\hat{\nabla}_\xi = \frac{\mathrm{i}}{\alpha}\bigg(\frac{4}{3}\sin(\xi\alpha) - \frac{1}{6}\sin(2\xi\alpha)\bigg)$$

and

$$\hat{\Delta}_\xi = \frac{1}{\alpha^2}\bigg(-\frac{5}{2} + \frac{8}{3}\cos(\xi\alpha) - \frac{1}{6}\cos(2\xi\alpha)\bigg),$$

respectively.

For $p = 3$, we define

$$\nabla F_n = \frac{1}{\alpha}\bigg(-\frac{1}{60}F_{n-3} + \frac{3}{20}F_{n-2} - \frac{3}{4}F_{n-1} + \frac{3}{4}F_{n+1} - \frac{3}{20}F_{n+2} + \frac{1}{60}F_{n+3}\bigg)$$

and

$$\Delta F_n = \frac{1}{\alpha^2}\bigg(\frac{1}{90}F_{n-3} - \frac{3}{20}F_{n-2} + \frac{3}{2}F_{n-1} - \frac{49}{18}F_n + \frac{3}{2}F_{n+1} - \frac{3}{20}F_{n+2} + \frac{1}{90}F_{n+3}\bigg).$$

The corresponding Fourier symbols are

$$\hat{\nabla}_\xi = \frac{\mathrm{i}}{\alpha}\bigg(\frac{3}{2}\sin(\xi\alpha) - \frac{3}{10}\sin(2\xi\alpha) + \frac{1}{30}\sin(3\xi\alpha)\bigg)$$

and

$$\hat{\Delta}_\xi = \frac{1}{\alpha^2}\bigg(-\frac{49}{18} + 3\cos(\xi\alpha) - \frac{3}{10}\cos(2\xi\alpha) + \frac{1}{45}\cos(3\xi\alpha)\bigg),$$

respectively.

The difference stencils for $p > 3$ may be found elsewhere [65].

References

[1] V. L. Ginzburg and L. D. Landau. *On the Theory of Superconductivity.* Springer Berlin Heidelberg, Berlin, Heidelberg, 2009.

[2] L. P. Gorkov. Microscopic derivation of the Ginzburg-Landau equations in the theory of superconductivity. *Journal of Experimental and Theoretical Physics*, 9(6):1364–1367, 1959.

[3] A. Schmid. A time dependent Ginzburg-Landau equation and its application to the problem of resistivity in the mixed state. *Physik der kondensierten Materie*, 5(4):302–317, 1966.

[4] S. J. Chapman, S. D. Howison, and J. R. Ockendon. Macroscopic models for superconductivity. *SIAM Review*, 34(4):529–560, 1992.

[5] I. S. Aranson and L. Kramer. The world of the complex Ginzburg–Landau equation. *Reviews of Modern Physics*, 74(1):99, 2002.

[6] V. García-Morales and K. Krischer. The complex Ginzburg–Landau equation: an introduction. *Contemporary Physics*, 53(2):79–95, 2012.

[7] M. C. Cross and P. C. Hohenberg. Pattern formation outside of equilibrium. *Reviews of Modern Physics*, 65(3):851, 1993.

[8] A. C. Newell, T. Passot, and J. Lega. Order parameter equations for patterns. *Annual Review of Fluid Mechanics*, 25(1):399–453, 1993.

[9] P. Coullet, L. Gil, and J. Lega. Defect-mediated turbulence. *Physical Review Letters*, 62(14):1619, 1989.

[10] D. Tanaka and Y. Kuramoto. Complex Ginzburg-Landau equation with nonlocal coupling. *Physical Review E*, 68(2):026219, 2003.

[11] V. García-Morales and K. Krischer. Nonlocal complex Ginzburg-Landau equation for electrochemical systems. *Physical Review Letters*, 100(5):054101, 2008.

[12] J. Denk, L. Huber, E. Reithmann, and E. Frey. Active curved polymers form vortex patterns on membranes. *Physical Review Letters*, 116(17):178301, 2016.

[13] T. H. Tan, J. Liu, P. W. Miller, M. Tekant, J. Dunkel, and N. Fakhri. Topological turbulence in the membrane of a living cell. *Nature Physics*, 16(6):657–662, 2020.

[14] A. C. Newell and J. A. Whitehead. Finite bandwidth, finite amplitude convection. *Journal of Fluid Mechanics*, 38(2):279–303, 1969.

[15] L. A. Segel. Distant side-walls cause slow amplitude modulation of cellular convection. *Journal of Fluid Mechanics*, 38(1):203–224, 1969.

[16] K. Stewartson and J. T. Stuart. A non-linear instability theory for a wave system in plane Poiseuille flow. *Journal of Fluid Mechanics*, 48(3):529–545, 1971.

[17] M. C. Cross. Derivation of the amplitude equation at the Rayleigh–Bénard instability. *Physics of Fluids*, 23(9):1727–1731, 1980.

[18] N. Stoop, R. Lagrange, D. Terwagne, P. M. Reis, and J. Dunkel. Curvature-induced symmetry breaking determines elastic surface patterns. *Nature Materials*, 14(3):337–342, 2015.

[19] T. Bohr, A. W. Pedersen, and M. H. Jensen. Transition to turbulence in a discrete Ginzburg-Landau model. *Physical Review A*, 42(6):3626, 1990.

[20] V. Hakim and W-J. Rappel. Dynamics of the globally coupled complex Ginzburg-Landau equation. *Physical Review A*, 46(12):R7347, 1992.

[21] J. F. Ravoux, S. Le Dizes, and P. Le Gal. Stability analysis of plane wave solutions of the discrete Ginzburg-Landau equation. *Physical Review E*, 61(1):390, 2000.

[22] K-I. Maruno, A. Ankiewicz, and N. Akhmediev. Exact localized and periodic solutions of the discrete complex Ginzburg–Landau equation. *Optics Communications*, 221(1-3):199–209, 2003.

[23] Y. Lv and J. Sun. Asymptotic behavior of stochastic discrete complex Ginzburg–Landau equations. *Physica D: Nonlinear Phenomena*, 221(2):157–169, 2006.

[24] S. J. Thomson, M. M. P. Couchman, and J. W. M. Bush. Collective vibrations of confined levitating droplets. *Physical Review Fluids*, 5:083601, Aug 2020.

[25] S. J. Thomson, M. Durey, and R. R. Rosales. Collective vibrations of a hydrodynamic active lattice. *Proceedings of the Royal Society A*, 476(2239), 2020.

[26] G. C Sethia and A. Sen. Chimera states: the existence criteria revisited. *Physical Review Letters*, 112(14):144101, 2014.

[27] B. Thakur and A. Sen. Collective dynamics of globally delay-coupled complex Ginzburg-Landau oscillators. *Chaos: an Interdisciplinary Journal of Nonlinear Science*, 29(5):053104, 2019.

[28] Y. Couder, S. Protiere, E. Fort, and A. Boudaoud. Walking and orbiting droplets. *Nature*, 437(7056):208–208, 2005.

[29] J. W. M. Bush. Pilot-wave hydrodynamics. *Annual Review of Fluid Mechanics*, 47:269–292, 2015.

[30] J. W. M. Bush, Y. Couder, T. Gilet, P. A. Milewski, and A. Nachbin. Introduction to focus issue on hydrodynamic quantum analogs. *Chaos: an Interdisciplinary Journal of Nonlinear Science*, 28(9):096001, 2018.

[31] J. W. M. Bush and A. U. Oza. Hydrodynamic quantum analogs. *Reports on Progress in Physics*, 2020.

[32] A. Eddi, E. Sultan, J. Moukhtar, E. Fort, M. Rossi, and Y. Couder. Information stored in Faraday waves: the origin of a path memory. *Journal of Fluid Mechanics*, 674:433–463, 2011.

[33] J. Moláček and J. W. M. Bush. Drops walking on a vibrating bath: towards a hydrodynamic pilot-wave theory. *Journal of Fluid Mechanics*, 727:612–647, 2013.

[34] P. J. Sáenz, G. Pucci, A. Goujon, T. Cristea-Platon, J. Dunkel, and J. W. M. Bush. Spin lattices of walking droplets. *Physical Review Fluids*, 3(10):100508, 2018.

[35] C. Bechinger, R. Di Leonardo, H. Löwen, C. Reichhardt, G. Volpe, and G. Volpe. Active particles in complex and crowded environments. *Reviews of Modern Physics*, 88(4):045006, 2016.

[36] C. Scholz, S. Jahanshahi, A. Ldov, and H. Löwen. Inertial delay of self-propelled particles. *Nature Communications*, 9(1):1–9, 2018.

[37] M. Leoni, M. Paoluzzi, S. Eldeen, A. Estrada, L. Nguyen, M. Alexandrescu, K. Sherb, and W. W. Ahmed. Surfing and crawling macroscopic active particles under strong confinement: Inertial dynamics. *Physical Review Research*, 2(4):043299, 2020.

[38] H. Löwen. Inertial effects of self-propelled particles: From active Brownian to active Langevin motion. *The Journal of Chemical Physics*, 152(4):040901, 2020.

[39] I. Ho, G. Pucci, A. U. Oza, and D. M. Harris. Capillary surfers: wave-driven particles at a fluid interface. *arXiv preprint arXiv:2102.11694*, 2021.

[40] M. C. Marchetti, J-F. Joanny, S. Ramaswamy, T. B. Liverpool, J. Prost, M. Rao, and R. A. Simha. Hydrodynamics of soft active matter. *Reviews of Modern Physics*, 85(3):1143, 2013.

[41] A. U. Oza, R. R. Rosales, and J. W. M. Bush. A trajectory equation for walking droplets: hydrodynamic pilot-wave theory. *Journal of Fluid Mechanics*, 737:552–570, 2013.

[42] S. H. Strogatz. *Nonlinear dynamics and chaos: with applications to physics, biology, chemistry, and engineering*. CRC press, Boca Raton, FL, 2018.

[43] J. K. Kevorkian and J. D. Cole. *Multiple scale and singular perturbation methods*, volume 114. Springer-Verlag, New York, NY, 2012.

[44] L. N. Trefethen. *Spectral Methods in MATLAB*. Society for Industrial and Applied Mathematics, Philadelphia, PA, 2000.

[45] C. R. Doering, J. D. Gibbon, D. D. Holm, and B. Nicolaenko. Low-dimensional behaviour in the complex Ginzburg-Landau equation. *Nonlinearity*, 1(2):279, 1988.

[46] M. Bartuccelli, P. Constantin, C. R. Doering, J. D. Gibbon, and M. Gisselfält. On the possibility of soft and hard turbulence in the complex Ginzburg-Landau equation. *Physica D: Nonlinear Phenomena*, 44(3):421–444, 1990.

[47] P. Coullet and S. Fauve. Propagative phase dynamics for systems with Galilean invariance. *Physical Review Letters*, 55(26):2857, 1985.

[48] P. C. Matthews and S. M. Cox. Pattern formation with a conservation law. *Nonlinearity*, 13(4):1293, 2000.

[49] N. L. Komarova and A. C. Newell. Nonlinear dynamics of sand banks and sand waves. *Journal of Fluid Mechanics*, 415:285–321, 2000.

[50] S. M. Cox and P. C. Matthews. New instabilities in two-dimensional rotating convection and magnetoconvection. *Physica D: Nonlinear Phenomena*, 149(3):210–229, 2001.

[51] T. B. Benjamin and J. E. Feir. The disintegration of wave trains on deep water. *Journal of Fluid Mechanics*, 27(3):417–430, 1967.

[52] J. T. Stuart and R. C. DiPrima. The Eckhaus and Benjamin-Feir resonance mechanisms. *Proceedings of the Royal Society of London. A: Mathematical and Physical Sciences*, 362(1708):27–41, 1978.

[53] P. A. Milewski and E. G. Tabak. A pseudospectral procedure for the solution of nonlinear wave equations with examples from free-surface flows. *SIAM Journal on Scientific Computing*, 21(3):1102–1114, 1999.

[54] N. K. Efremidis and D. N. Christodoulides. Discrete Ginzburg-Landau solitons. *Physical Review E*, 67(2):026606, 2003.

[55] M. G. Clerc, R. G. Elías, and R. G. Rojas. Continuous description of lattice discreteness effects in front propagation. *Philosophical Transactions of the Royal Society A: Mathematical, Physical and Engineering Sciences*, 369(1935):412–424, 2011.

[56] P. C. Matthews and H. Susanto. Variational approximations to homoclinic snaking in continuous and discrete systems. *Physical Review E*, 84(6):066207, 2011.

[57] M. Durey, P. A. Milewski, and Z. Wang. Faraday pilot-wave dynamics in a circular corral. *Journal of Fluid Mechanics*, 891:A3, 2020.

[58] D. M. Abrams and S. H. Strogatz. Chimera states for coupled oscillators. *Physical Review Letters*, 93(17):174102, 2004.

[59] G. C. Sethia, A. Sen, and F. M. Atay. Clustered chimera states in delay-coupled oscillator systems. *Physical Review Letters*, 100(14):144102, 2008.

[60] S. Nkomo, M. R. Tinsley, and K. Showalter. Chimera states in populations of nonlocally coupled chemical oscillators. *Physical Review Letters*, 110(24):244102, 2013.

[61] E. A. Martens, S. Thutupalli, A. Fourrière, and O. Hallatschek. Chimera states in mechanical oscillator networks. *Proceedings of the National Academy of Sciences*, 110(26):10563–10567, 2013.

[62] J. Wojewoda, K. Czolczynski, Y. Maistrenko, and T. Kapitaniak. The smallest chimera state for coupled pendula. *Scientific Reports*, 6(1):1–5, 2016.

[63] J. F. Totz, J. Rode, M. R. Tinsley, K. Showalter, and H. Engel. Spiral wave chimera states in large populations of coupled chemical oscillators. *Nature Physics*, 14(3):282–285, 2018.

[64] J. Denk and E. Frey. Pattern-induced local symmetry breaking in active-matter systems. *Proceedings of the National Academy of Sciences*, 117(50):31623–31630, 2020.

[65] M. Abramowitz, I. A. Stegun, and R. H. Romer. Handbook of mathematical functions with formulas, graphs, and mathematical tables. *American Journal of Physics*, 56(10):958–958, 1988.